Astronomy & Astrophysics manuscript no. output
November 12, 2026
©ESO 2026

Euclid Data Release 1 (DR1)

The PHZ processing function for the physical properties of galaxies.

Euclid Collaboration: A. Enia, W. G. Hartley, M. Bolzonella, F. Dubath, S. Paltani, L. Pozzetti, C. Saulder, M. Tucci, et al.

(Full author list and affiliations details can be found after the references)

November 12, 2026

ABSTRACT

Euclid is a European Space Agency mission mapping the extragalactic sky, aiming to provide the most-accurate 3D view of the Universe at optical and near-infrared wavelengths, by measuring the photometric redshifts of billions of galaxies. Within the Euclid Consortium, this task is executed by the PHZ Organisation Unit. PHZ takes as input the multi-wavelength photometry of *Euclid* and ground-based data, and returns as output the source classification, photometric redshifts for the *Euclid* core science (i.e., cosmology), and photometric redshifts plus physical parameters and absolute magnitudes for non-cosmological science. As part of the first Euclid Data Release (DR1), we describe the details of the DR1 pipeline for non-cosmological science, along with the released data products, and their validation. The non-cosmological science data products are obtained with `NNPZ`, a nearest-neighbour algorithm developed within PHZ that infers the properties of each target galaxy from its closest matches, in colour–magnitude space, within a reference sample of galaxies with known redshifts and physical parameters. We built this reference sample from *Euclid* observations of COSMOS, one of the Euclid Auxiliary Fields, labelling each galaxy with redshifts and physical parameters derived from the COSMOS2020 multi-wavelength photometry, consistently with the *Euclid* core-science results. Combined with the adjustments and priors required to generalise the results across the entire extragalactic sky, this approach yields high-quality and internally consistent data products. We tested the performance using both internal metrics and comparisons to ancillary data sets (e.g., COSMOS2020, 3D-HST, and DESI) and scaling relations (e.g., the star-forming main sequence); the results are in line with expectations and pre-DR1 simulations for both the Euclid Wide Survey and Euclid Deep Fields.

Key words. Methods: data analysis — Catalogues — Galaxies: evolution — Galaxies: formation — Galaxies: fundamental parameters — Galaxies: statistics

1. Introduction

Euclid is a European Space Agency mission designed to map the large-scale distribution of matter in the Universe. The spacecraft carries two instruments: the visible imaging instrument (VIS, Euclid Collaboration: Cropper et al. 2025) and the Near-Infrared (NIR) Spectrometer and Photometer (NISP, Euclid Collaboration: Jahnke et al. 2025), which together provide high-resolution optical imaging and NIR imaging and spectroscopy over approximately 11 000 deg^2 of the extragalactic sky, the Euclid Wide Survey (EWS). At the end of the nominal mission, the EWS will reach a uniform depth of 24.5 AB magnitudes in the visible band and fainter than 24.0 in the NIR bands (Euclid Collaboration: Scaramella et al. 2022). Although *Euclid* was primarily designed to constrain dark energy and dark matter through weak gravitational lensing and galaxy clustering, the resulting data set is a substantial resource for non-cosmological science as well (Euclid Collaboration: Mellier et al. 2025).

Achieving the mission's full scientific potential requires photometric redshifts – or photo-zs – for billions of galaxies. These will be used both to reconstruct the three-dimensional distribution of matter and to trace galaxy evolution across a wide range of cosmic time. To meet the required precision, *Euclid* incorporates multi-band photometry from ground-based surveys, including the Dark Energy Survey (DES, Flaugher et al. 2015; DES Collaboration: Abbott et al. 2016), the Ultraviolet Near Infrared Optical Northern Survey (UNIONS, Gwyn et al. 2025), and, in future, the Legacy Survey of Space and Time (LSST, Ivezic et al. 2008).

The processing of these data is managed by the Euclid Science Ground Segment (SGS), organised into self-contained processing functions (PFs). The PHZ PF is responsible for photometric redshifts, physical parameters (PPs) of galaxies, source classification, spectral energy distribution (SED) estimation, and tomographic binning. The PPs – stellar masses, star-formation rates (SFR), metallicities, and others – are central to the non-cosmological science cases that aim to reconstruct the assembly history of the Universe. For this purpose, PHZ developed a machine-learning algorithm, the Nearest-Neighbour Photometric Redshifts (`NNPZ`, Tanaka et al. 2018; Euclid Collaboration: Enia et al. 2024; Euclid Collaboration: Tucci et al. 2026; Euclid Collaboration: Enia et al. 2026). `NNPZ` estimates multi-dimensional posterior distributions of photo-zs and PPs by searching, in colour–magnitude space, for the nearest neighbours of each target galaxy within a pre-defined reference sample of objects with known properties.

In this paper, we describe the PHZ pipeline for photometric redshifts and galaxy PPs used for the first $\sim$ 1900 deg^2 of the Euclid Data Release 1 (2026). The accuracy and precision of the released data products are validated against large spectroscopic samples from external surveys, demonstrating their reliability for a broad range of astrophysical applications. This paper is structured as follows. In Sect. 2, we describe the DR1 data and the ancillary data sets used to evaluate performance.

Table 1. Filters for the Euclid DR1, with associated observed depths.

Band	$\lambda_{\rm eff}$ [µm]	EWS $\sim 1900\,{\rm deg}^2$	EDF-N $\sim 20\,{\rm deg}^2$	EDF-F $\sim 10\,{\rm deg}^2$	EDF-S $\sim 20\,{\rm deg}^2$	PV-005 $\sim 1\,{\rm deg}^2$	CDFS $\sim 0.1\,{\rm deg}^2$
$u_{\rm CFHT/MegaCam}$	0.372	23.2[a]					
$r_{\rm CFHT/MegaCam}$	0.640	24.0					
$i_{\rm PAN-STARRS}$	0.755	23.6					
$g_{\rm HSC}$	0.480	24.5	26.4	26.4		27.2	26.8
$r_{\rm HSC}$	0.640		26.1			26.5	
$r2_{\rm HSC}$	0.640		26.0	25.4		26.5	26.6
$i_{\rm HSC}$	0.755		24.9	25.0		26.4	25.2
$i2_{\rm HSC}$	0.755		25.5	25.7		24.8	26.2
$z_{\rm HSC}$	0.891	23.0	24.9	24.6		26.3	25.0
$g_{\rm Decam}$	0.473	24.7		26.1	24.7	26.6	26.8
$r_{\rm Decam}$	0.642	24.3		25.8	24.3	25.9	26.9
$i_{\rm Decam}$	0.784	23.8		25.5	23.7	25.7	26.7
$z_{\rm Decam}$	0.926	23.0		25.1	23.0	24.2	26.3
VIS/$I_{\rm E}$	0.715	24.8	26.2	24.9	25.8	26.2	26.4
NISP/$Y_{\rm E}$	1.081	23.2	24.5	23.4	24.3	24.7	24.8
NISP/$J_{\rm E}$	1.367	23.3	24.7	23.5	24.4	24.8	25.0
NISP/$H_{\rm E}$	1.771	23.3	24.7	23.5	24.4	24.8	25.0

Notes. Reported magnitudes are the $10\,\sigma$ observed median depths of the observing tiles for an extended source in a $2\times$FWHM diameter aperture. As a rule-of-thumb, the $5\,\sigma$ median depths are obtained by adding 0.75 mag.
[(a)] The $u_{\rm CFHT/MegaCam}$ band for the EWS in the northern sky is only available for roughly half of the EWS-N, and not for the EDF-N.

In Sect. 3, we describe the PHZ pipeline for recovering photo-zs and PPs for non-cosmological science, and the products stored in the Euclid Archive System (EAS, Euclid Collaboration: Aussel et al. 2026). In Sect. 4, we validate the results against spectroscopic redshifts and Hα-estimated SFRs, while checking the relation between stellar masses and SFR, the star-forming main-sequence (SFMS). In Sect. 5, we present our conclusions.

All the results described in this work assume a flat cosmological-constant-dominated cold dark matter (ΛCDM) cosmology with $H_0 = 67.74\,{\rm km\,s^{-1}\,Mpc^{-1}}$, $\Omega_{\rm m} = 0.3089$, and $\Omega_\Lambda = 0.6911$ (Planck Collaboration et al. 2016), and assume a Chabrier (2003) initial mass function (IMF). All magnitudes are given in the AB photometric system (Oke & Gunn 1983).

2. Data

A comprehensive view of all the scientific objectives of the *Euclid* mission is presented in Euclid Collaboration: Mellier et al. (2025). A detailed description of Data Release 1 (DR1) is available in Euclid Collaboration: Aussel et al. (2026); here we provide a brief summary.

Euclid DR1 is composed of approximately $1900\,{\rm deg}^2$ of the extragalactic sky, broadly divided into the EWS, the Euclid Deep Fields (EDFs), and the Euclid Auxiliary Fields (EAFs). The EDFs are composed of three fields: EDF-North (EDF-N), EDF-Fornax (EDF-F), and EDF-South (EDF-S), while the EAFs are a series of well-known extragalactic fields (further details available in Euclid Collaboration: Aussel et al. 2026; Euclid Collaboration: Tereno et al. 2026).[1] *Euclid* observed all the DR1 footprint in four photometric bands, one in the visible ($I_{\rm E}$, Euclid Collaboration: Cropper et al. 2025), and three in the NIR ($Y_{\rm E}$, $J_{\rm E}$, and $H_{\rm E}$, Euclid Collaboration: Jahnke et al. 2025). *Euclid* observations are complemented by ground-based observations carried out with multiple instruments to cover the wavelength range between 0.3 µm and 1.8 µm by the Ultraviolet Near-Infrared Optical Northern Survey (UNIONS, Gwyn et al. 2025) in the northern hemisphere; in the southern hemisphere, *Euclid* is complemented with observations made by the Dark Energy Survey (DES, Flaugher et al. 2015; DES Collaboration: Abbott et al. 2016). In the EDFs and EAFs, other deeper ground-based observations are available, namely the Hawaii $20\,{\rm deg}^2$ survey (H20, Euclid Collaboration: McPartland et al. 2025). Euclid DR1 will also contain *Euclid* NISP spectroscopic redshifts and spectral line measurements (Euclid Collaboration: Scodeggio et al. 2026; Euclid Collaboration: Fumana et al. 2026).

While the EWS covers the sky with a series of single reference observation sequences (ROS, in Figure 8 of Euclid Collaboration: Scaramella et al. 2022), in contiguous $32' \times 32'$ "tiles", the EAFs and EDFs have been observed multiple times with varying depth in tiles of $17' \times 17'$: EDF-F has been observed two times, with an expected improvement in depth of 0.4 magnitudes with respect to the EWS; EDF-S ten times (1 mag deeper), and EDF-N eleven times (the same). The depths of the different EAFs depend instead on different factors (e.g., zodiacal background). All the inputs for the PHZ pipeline come from the MER processing function, described in Euclid Collaboration: Kümmel et al. (2026). Each catalogue contains all the objects detected in $I_{\rm E}$ (Euclid Collaboration: McCracken et al. 2026) or in a NIR-stacked detection image that is the combination of $Y_{\rm E}$, $J_{\rm E}$, and $H_{\rm E}$ (Euclid Collaboration: Polenta et al. 2026). There are ~ 9000 tiles in DR1, with a total of 880 955 708 unique detected sources, 30 809 240 in the EDFs and 850 146 468 in the EWS.

For the photometry, for each detected source in a given tile, there are three main sets of measurements: aperture-, model-, and template-fitting photometry. Within PHZ, we are interested in the total emission of the source, while preserving the measurement of colours belonging to the same physical region of each galaxy. For VIS and NIR-stacked images we used the total flux computed within a Kron aperture with the A-PHOT algorithm (Merlin et al. 2015, 2016). For all the other bands, the total flux

[1] See also https://www.cosmos.esa.int/web/euclid/euclid-dr1-expected-coverage for the exact sky coverage and position of the fields in DR1.

is obtained by scaling with a colour term,

$$F^{\rm total}_{\rm band} = F^{\rm total}_{\rm detection} \times \frac{F^{\rm aperture}_{\rm band}}{F^{\rm aperture}_{\rm detection}} \quad (1)$$

where $F^{\rm aperture}_{\rm band}$ is the aperture flux measured in the band of interest, and $F^{\rm aperture}_{\rm detection}$ is the aperture flux measured in the detection image, whether $I_{\rm E}$ or the NIR-stacked image. Both aperture fluxes are measured on images degraded to the worst resolution among the bands considered. As input to PHZ, we used the flux measured in a circular aperture of diameter $2 \times$ FWHM, converted to total flux. In Table 1 we report the filters used in this work, with the observed $10\,\sigma$ depths for an extended source in an aperture whose diameter is twice the FWHM from the lowest resolution band between the optical and *Euclid* ones (further details on the photometry in Euclid Collaboration: Corcho-Caballero et al. 2026; Euclid Collaboration: Kümmel et al. 2026; Euclid Collaboration: Gasparetto et al. 2026).

When reporting the results in Sect. 4, we applied a series of quality cuts to make the analysis more robust, removing low-quality sources. These are:

- `SPURIOUS_FLAG` = 0;
- `DET_QUALITY_FLAG` < 4;
- `MUMAX_MINUS_MAG` > −2.6.

This selection removes low-quality objects from the sample, as well as stars and compact objects, e.g., QSOs. For details on the meaning of the flags, see Euclid Collaboration: Kümmel et al. (2026).

We further cleaned our sample looking for reliable extragalactic sources with both the PHZ source classification of the DR1 data products and the `NNPZ` flag on the recovered photo-z and PPs, imposing:

- `PHZ_CLASSIFICATION` = 2;
- `PHYS_PARAM_FLAGS` = 0.

The first condition selects sources that have been classified as galaxies, while with the second we select only those sources with at least a nearest-neighbour in the reference sample with a weight higher than 10^{-3} (see Euclid Collaboration: Hartley et al. 2026, and Sect. 3 for further details on the pipeline).

Additionally, we applied an $H_{\rm E}$ magnitude cut that limits the signal-to-noise ratio (S/N, measured in an aperture of $2\times$ FWHM diameter) to five. We warn the reader that the above described selection was chosen only for the validation of the DR1 products, and it is not intended as the blueprint for the different scientific studies that can be done with DR1 data. To give an example, for statistical studies that require a rigorous definition of the survey area, the *Euclid* photometric visibility mask PhotoZ (VMPZ, see Euclid Collaboration: Odier et al. 2026) are better suited. We also note that the above selection, by requiring `PHZ_CLASSIFICATION = 2` and removing compact, non-stellar sources (via `MUMAX_MINUS_MAG` cut), effectively restricts our validation sample to extended objects only. We therefore assumed that all extended sources are galaxies, ignoring the fact that some of them are in fact AGNs. The performance of the PHZ pipeline for AGN and QSO-classified objects is not discussed in this work.

In order to assess the quality of the photometric redshifts and PPs (e.g., stellar masses or SFRs), we compared them with the available literature compilations of spectroscopic redshifts and (when available) high-quality PPs, whether because they have been measured with a large number of photometric points or with spectral line information available. The EDFs are the part of the Euclid DR1 with the most coverage from other extragalactic spectroscopic surveys. A full list of references for high-quality spec-z galaxies that matches with the *Euclid* observations is available in Euclid Collaboration: Hartley et al. (2026), Euclid Collaboration: Enia et al. (2026), or in Table 5 of Euclid Collaboration: Tucci et al. (2026). We compared these with the results of the Deep Pipeline for the EDFs and of the single EWS-like passes of the same fields, in order to assess the quality of the results for the EWS. Despite being the deepest, with ten ROSs, only a handful of reliable spectroscopic redshifts are available within the EDF-S; therefore, in the following sections we do not show for EDF-S the full set of tests that we performed for the EAFs, EDF-N, and EDF-F, and we limit our report of the EDF-S metrics to Table 4.

Given the technical details on how the PHZ results for non-cosmological science have been measured, a field of extreme importance is the Cosmic Evolution Survey (COSMOS). The latest release (COSMOS2020, Weaver et al. 2022) was used within PHZ to build the reference samples (described in Sect. 3 and Euclid Collaboration: Hartley et al. 2026). In this work, we also used it to compare photo-zs and PPs with what can be seen as the best quality available stellar masses and SFRs, both for validating the reference sample, and as part of the Performance Verification 005 field (see Sect. 4.2), an EAF covering the innermost part of COSMOS. In COSMOS, we also compared our results with the compilation of available spectroscopic redshifts in Khostovan et al. (2026) with redshift quality $Q_{\rm f} = 4$. For the EAF Chandra Deep Field South (CDFS), we compared them with the 3D-HST compilation of spectroscopic redshifts and PPs (van Dokkum et al. 2013; Momcheva et al. 2016).

Finally, for a limited sample of approximately 5000 sources within $0 < z < 0.6$, we compared the measured SFRs with those reported in the value-added catalogue of PPs for the Dark Energy Spectroscopic Instrument (DESI, DESI Collaboration: Aghamousa et al. 2016; Siudek et al. 2024). Specifically, we used SFRs derived from both the Hα and Hβ emission lines following Kennicutt (1998). Although these estimates are not as reliable as spectroscopic redshifts for establishing the 'ground truth', they are sufficiently accurate to provide an indication of the quality of the recovered SFRs, at least in the South.

3. OU-PHZ pipeline for physical parameters

A more complete overview of the full OU-PHZ pipeline for DR1 is given in Euclid Collaboration: Hartley et al. (2026). In this section, we complement that with a specific focus on photometric redshifts and PPs for non-cosmological science, with galaxies being the main focus. In fact, as shown in Figure 1 of Euclid Collaboration: Hartley et al. (2026), the PHZ production pipeline is broadly divided into two branches: the core-science branch (e.g., cosmology and weak-lensing, described in Sections 7 and 8 of Euclid Collaboration: Mellier et al. 2025) and the non-cosmological science branch (e.g., extragalactic astrophysics, see Section 9 of the *Euclid* overview paper). Both branches are intertwined, relying on the same inputs and – for PPs – from outputs of the core-science branch; as such, at least a short summary of both is needed to gain full comprehension of the PHZ data products for our purposes.

Given the large number of detected sources (see Sect. 2), machine learning (ML) methods have been extensively tested and then used within PHZ to speed up the computational process, while achieving a performance comparable to template fitting methods (see e.g., Euclid Collaboration: Desprez et al.

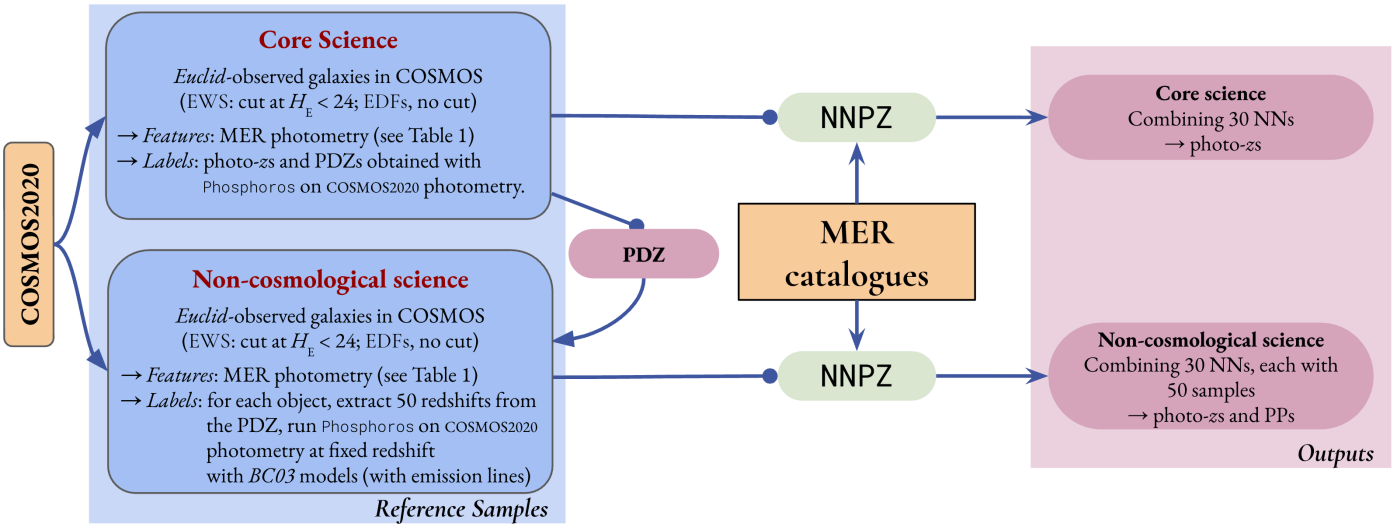


Fig. 1. Schematic view of the PHZ pipeline for the core and non-cosmological science, where the PPs are measured. The pipeline inputs are within orange boxes, outputs are in pink, and specific tasks in green. Both reference samples are built running `Phosphoros` on COSMOS2020 photometry. The output PDZs obtained when finding the labels for the core-science reference sample are used as an input for building the labels for the non-cosmological science reference sample: 50 redshifts are randomly extracted from the PDZ, and used to run `Phosphoros` at fixed redshift to infer the PPs and absolute magnitudes. After the `NNPZ` run, the 30 NNs are used to infer the outputs both for core-science (only photo-zs) and non-cosmological science, where each NN will have 50 samples attached from the `Phosphoros` run described above. Further details available in Euclid Collaboration: Hartley et al. (2026) and Sect. 3.

Table 2. Summary of all the PHZ pipeline output. The meaning of these parameters is described in Sect. 3 and in Euclid Collaboration: Hartley et al. (2026).

File Name	Description.
`PHZCAT`	Core science results: photo-zs and PDZs.
`PPSAMPLINGINDEX`	Indices, weights, and scaling factors of the 30 NNs.
`PPSAMPLINGFILE`	Non-cosmological science results: 50 samples from the combined posterior distribution functions (PDFs) of all the NNs.
`PHYSPARAM`	Non-cosmological science results: median, mode, and percentiles of all the quantities in Table 3.
`PHYSPARAMNIR`	`Phosphoros` results on NISP-detected galaxies; only photo-zs and PDZs.
`PHYSPARAMQSO`	`Phosphoros` results on QSO-classified objects; only photo-zs and PDZs.
`CLASSCAT`	Results from the classification pipeline for galaxies.
`STARCLASS`	Results from the classification pipeline for stars.

Table 3. Summary of physical parameters provided in the Euclid DR1 PHZ pipeline output.

Property	Units / Scale
Stellar Population	
`STELLARMASS`	$\log_{10}(M_*/M_\odot)$
`SFR`	$\log_{10}(\mathrm{SFR}/M_\odot\,\mathrm{yr}^{-1})$
`MASSFORMED`	$\log_{10}(M_*/M_\odot)$
`SFHAGE`	Gyr
`SFHTIMESCALE`	Gyr
`STELLARMETALLICITY`	$Z/Z_\odot$
Dust	
`AV`	mag
Absolute Magnitudes	
`M_VIS`	mag
`M_[FUV, NUV, U, B, V]`	mag
`M_[R, I, Z]`	mag
`M_[Y, J, H, KS]`	mag

Notes. Each parameter includes associated median, mode, and 68% confidence intervals derived from the PDFs.

2020; Euclid Collaboration: Enia et al. 2024). As for the non-cosmological pipeline for Quick Data Release 1 (Q1), the DR1 science data products were obtained using a nearest-neighbours (NNs) algorithm, called `NNPZ`. First described in Tanaka et al. (2018), and later developed within PHZ, `NNPZ` works by searching for each target galaxy a k number of NNs in the features space (i.e., magnitude and colour) from a previously defined reference sample. In the *Euclid* pipeline, the number of NNs was set to 30, the optimal compromise between a reliable inference of photo-zs and PPs, and the computational cost of storing the NNs information. The NNs have their own weights – measured from the χ^2 distance between the reference and the target – and scaling parameters from the SED amplitude. For each target source, the 30 neighbours are combined to infer its labels, i.e., the median (or the mode) of the (weighted) distribution of NNs; these are ultimately the inferred photo-zs, PPs, and absolute magnitudes of the target galaxies. The same approach is employed in the core-science branch of the PHZ pipeline, where the photometric redshifts are the lone labels attached to the reference sample, and thus the only quantity measured in the process. This is a key difference from what was done for Q1, when the core-science

photometric redshifts were measured using Phosphoros (Euclid Collaboration: Tucci et al. 2026).

Another difference from Q1 is in the definition and construction of the reference sample. In Q1, the reference sample was built from a grid of templates and exponentially delayed star-formation histories (see Section 6.1 of Euclid Collaboration: Tucci et al. 2026, or Section 3 of Euclid Collaboration: Enia et al. 2026). For DR1, observations of the EAFs are available, thus making it possible to build the reference sample from a catalogue of real, observed galaxies, rather than a grid of templates. For both branches, we built the reference sample from *Euclid* observations of COSMOS, one of the EAFs. There are in fact two different versions of the reference sample, depending on whether it is used for the processing of the EWS or the processing for the EDFs. In practice, we built the samples by matching the Euclid DR1 observations of COSMOS with the COSMOS2020 catalogue – including *Euclid*, DES, and HSC bands – cut in magnitude at a depth similar to that of the *Euclid* data to which they were applied. For the EWS, the reference sample is made of $\sim$ 375 k galaxies cut at $H_{\rm E} < 24$ or $I_{\rm E} < 25$; for the EDFs, the reference sample is made of $\sim$ 630 k galaxies, without any cut in magnitude (or, cut at the implicit UltraVISTA H-band limit in COSMOS).

In both cases, the reference sample labels (i.e., the photo-zs) were not taken directly from the COSMOS2020 catalogue, but were measured from a dedicated Phosphoros run on the available COSMOS2020 photometry (from the Classic catalogue, see Table 3 in Euclid Collaboration: Hartley et al. 2026), ranging from u to K bands, and then cross-matched with the *Euclid* MER catalogue in the same field, to attach the *Euclid* observations as features in the reference sample. In building the core-science branch reference sample, the Phosphoros templates were obtained from an interpolation of 33 SED-models, including emission lines, looking for the best-fit photometric redshifts (more details in Euclid Collaboration: Hartley et al. 2026), with a volume prior applied. The outcome of the run is a reference sample whose features are the *Euclid*, DES, UNIONS, and HSC bands (for the EDFs), and the Phosphoros-measured photo-zs as associated labels, and it is used in NNPZ to evaluate the core-science results.

We constructed the non-cosmological science reference sample as follows. In order to associate the PPs and absolute magnitudes with each reference source along with photo-zs, we drew 50 random redshifts from the PDZ of the above mentioned Phosphoros run, and executed another dedicated run of Phosphoros at fixed redshift on the COSMOS2020 photometries – this time also including the first two channels of IRAC, see Table 3 in Euclid Collaboration: Hartley et al. (2026) – obtaining a set of PPs and absolute magnitudes. As such, each reference source has 50 different realisations with their own photometric redshifts and correlated PPs and absolute magnitudes. This procedure ensures a high level of internal consistency between the core science products and the non-cosmological science results. The models used in Phosphoros are a set of Bruzual & Charlot (2003, 2016 version[2]) templates using the MILES stellar library, with added emission lines; following what has been done in Euclid Collaboration: Enia et al. (2026), and addressing some issues already found in Q1 (see Section 6.1.1 of Euclid Collaboration: Tucci et al. 2026), we removed models with unrealistically young ages – $\log_{10}(T_0/{\rm yr}) < 8$ – and implemented a complex grid of templates in steps of d$z = 0.01$, accounting for a redshift-dependent age prior.

[2] http://www.bruzual.org/bc03/Updated_version_2016/

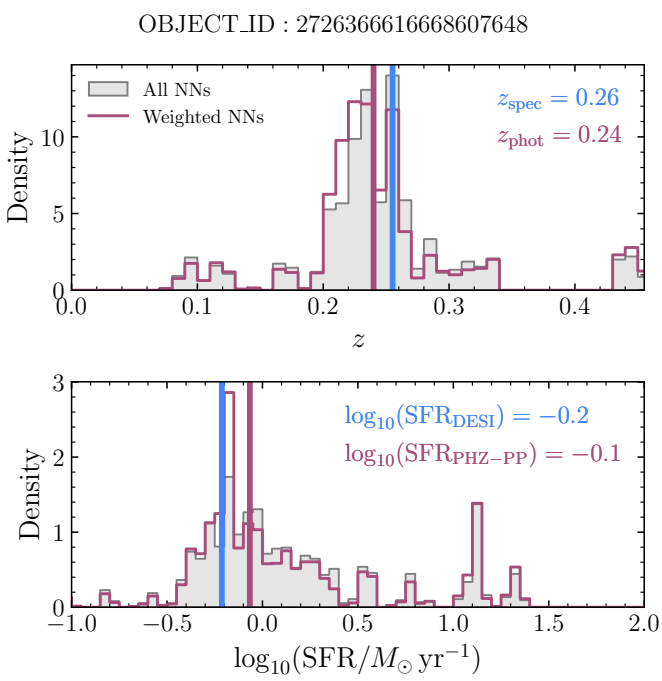


Fig. 2. Example of the NNPZ output for a galaxy in EDF-N. The grey histogram is the distribution of all the NN, while the purple one is the one weighted with the product of the χ^2-distance-inferred weight and the intrinsic one to smooth out cosmic structures in COSMOS (see Sect. 3). In blue we report the DESI measured spectroscopic redshift and SFR obtained from observations of Hα and Hβ emission lines, and in pink, the (median) PHZ inferred value.

One of the main setbacks of such an ML-based approach is the risk of overfitting the available reference data: in *Euclid*, it would mean replicating what is found in 2 deg^2 of COSMOS on the whole 1900 deg^2 of the extragalactic sky in DR1. For example, the existence of large-scale structures in COSMOS must be smoothed out when searching for the redshifts of galaxies in the rest of the sky. It might also be possible that extremely massive galaxies not present in COSMOS with $\log_{10}(M_*/M_\odot) \geq 12.5$ (e.g., Section 10.3 in Euclid Collaboration: Mellier et al. 2025) do actually exist in the whole $\sim$ 11 000 deg^2 of the survey. Different measures were taken within PHZ to mitigate and eliminate these potential problems.

The first is a weight[3] that is applied to all the objects in the reference sample, acting as a multiplicative prior for each NN. This slightly underweights some COSMOS-related redshift structures while favouring others. The weighting scheme is applied both for the core and the non-cosmological science part of the pipeline. Further details can be found in Euclid Collaboration: Hartley et al. (2026).

The second is a factor that accounts for the SED amplitude scalings between the observed and reference sample colours. For each NN, there is an associated scaling factor, which enters the evaluation of PPs. For example, a galaxy with an important scaling between the reference sample's combined NNs $H_{\rm E}$ magnitudes and its own observed $H_{\rm E}$ magnitude will see its stellar mass properly scaled with respect to the one coming straight from the combination of the weighted NNs, allowing NNPZ to find objects with extremely high stellar masses that are not actually

[3] This is another weight, not to be confounded with the χ^2 weight assigned to the 30 NNs, to which is it multiplied when inferring the photo-zs and PPs.

present in the reference sample. In Q1, the scaling factor was left free to vary, generating some troubling cases where wrong redshift attributions (particularly low-z galaxies misplaced at high-z) artificially inflated the stellar masses to unphysical values $\log_{10}(M_*/M_\odot) > 14$. For DR1, the allowed values for the scaling factor are not completely free, but follow a lognormal distribution, substantially decreasing the presence of such outliers.

The pipeline takes as input the tile-by-tile source catalogues generated by the MER PF. These include all objects detected in the I_E images or in the NIR-stacked images combining the Y_E, J_E, and H_E data (further details available in Euclid Collaboration: Kümmel et al. 2026, and Sect. 2 for how these have been ingested in PHZ). What is inside the final data product of the non-cosmological science PHZ pipeline is dictated by the Euclid DR1 Data Model (DMDR1).[4] The DMDR1 guarantees uniformity and compatibility among the different Level 3 (LE3) science products, strictly defining the content of the PPs catalogue. In addition to dictating the particular PPs to be estimated (e.g., stellar mass, SFR, and dust attenuation), it also specifies the statistical estimators needed for each, which are the median, mode, and 68% confidence intervals obtained from the PDFs. These outputs are stored in all the files named `PHYSPARAM`. Also, files containing the indices of the reference sample NNs, weights, and scaling factor for each galaxy are available (`PPSAMPLINGINDEX`); finally, files with 50 samples for each parameter, extracted from the full PDFs, are also available in the SAS (`PPSAMPLINGFILE`, only for the Deep Processing). A summary of all the PHZ release output files is given in Table 2, while an overview of the PPs released in compliance with the DMDR1 is summarised in Table 3. Among the less immediately obvious parameters, `SFHAGE` refers to the age of the galaxy (i.e., the time elapsed since the onset of star formation), `SFHTIMESCALE` is the characteristic timescale of the star-formation history, usually identified as the τ parameter, and `MASSFORMED` is the total stellar mass ever formed. In Fig. 2 we show an example of an `NNPZ` output for a galaxy in the EDF-N, limited to z and SFR. The distributions of the unweighted and weighted NNs are reported there, where we also report a comparison with the known z_{spec} and SFR from Hα and Hβ measurements in DESI.

4. Validation

In this section we describe and validate the DR1 data products. We do this by comparing with well-known, state-of-the-art ancillary data, and quantifying the performance using a common set of metrics.

4.1. Metrics for quality assessment

Following what has already been implemented in Euclid Collaboration: Enia et al. (2026), to quantify the performance we define a uniform set of metrics, with some slight differences when referring to redshifts or PPs. Here we report their definitions and refer the reader to Euclid Collaboration: Enia et al. (2024) for a full discussion on the chosen thresholds and the catastrophic outlier definition.

We define the normalised median absolute deviation as

$$\mathrm{NMAD} = 1.48 \times \mathrm{median} \begin{cases} \dfrac{|z_{\rm pred} - z_{\rm test}|}{1 + z_{\rm test}} - b\,, & \text{for redshifts,} \\ |y_{\rm pred} - y_{\rm test}| - b\,, & \text{for PPs,} \end{cases} \quad (2)$$

with b being the model bias (see below). The outlier fraction is defined as

$$f_{\rm out} = \begin{cases} \dfrac{|z_{\rm pred} - z_{\rm test}|}{1 + z_{\rm test}} > 0.15\,, & \text{for redshifts,} \\ |y_{\rm pred} - y_{\rm test}| > t_{\rm out}\,, & \text{for PPs,} \end{cases} \quad (3)$$

with $t_{\rm out} = 0.4$ for stellar masses and $t_{\rm out} = 0.8$ for SFR. We define the bias as

$$b = \mathrm{median} \begin{cases} \left(\dfrac{z_{\rm pred} - z_{\rm test}}{1 + z_{\rm test}}\right), & \text{for redshifts,} \\ (y_{\rm pred} - y_{\rm test})\,, & \text{for PPs.} \end{cases} \quad (4)$$

In all of those cases, we compare a set of true values $z_{\rm test}$ and $y_{\rm test}$, with predicted values $z_{\rm pred}$ and $y_{\rm pred}$ (on a logarithmic scale for PPs).

Finally, we also quantify the information on the quality of the PDFs with the probability integral transform (PIT, Dawid 1984; D'Isanto & Polsterer 2018). PIT measures the overall distribution of the cumulative distribution functions of a parameter θ, $p(\theta)$, measured at its true values $\theta_{\rm true}$

$$\mathrm{PIT} = \int_{-\infty}^{\theta_{\rm true}} p(\theta)\,\mathrm{d}\theta\,, \quad (5)$$

where θ might be either photometric redshifts (in that case, $\theta_{\rm true} = z_{\rm spec}$) or a generic physical parameter (e.g., SFRs, with $\theta_{\rm true}$ being SFR measured from all the spectral information coming from the Hα and Hβ emission lines). When these correctly reproduce the PDF of the sources, the PIT is flat. A concave, U-shaped PIT signals an underestimation of the width of the PDFs (and thus, the associated errors); the opposite, a convex-shaped PIT, signals an overestimation. Outliers appear as peaks (i.e., PIT equal to 0 or 1) at the edges of the distribution. Biases in the recovered quantities show up in the PIT as an asymmetry with respect to a flat shape.

4.2. Reference sample and auxiliary fields

As a first necessary step to assess the quality of the PHZ data products, we must determine how well the reference sample was built, and how representative it is of the whole generic population. As reported in Sect. 3, the reference sample for non-cosmological science was obtained from a `Phosphoros` run of all *Euclid* observed galaxies in COSMOS2020 with BC03 models, for each galaxy at 50 fixed redshifts, which are extracted from the PDZ of the `Phosphoros` run made to construct the core-science reference sample. These labels were then associated with each reference sample object, having the *Euclid* observations of the field as features. There are two reference samples, one for the EDFs, with 628 281 galaxies, and one for the EWS, obtained from the former with a cut in $H_E < 24$ or $I_E < 25$, with 374 829 galaxies.

COSMOS is one of the most well-known fields in the extragalactic sky, with a considerable amount of multi-wavelength observations able to constrain photometric redshifts and PPs at the state-of-the-art level. We compared the labels we obtained for the reference sample with the compilation of spectroscopic redshifts in COSMOS by Khostovan et al. (2026) – the unique sources catalogue – as ground-truth for the redshifts, and the best-fit `LePhare` results from the COSMOS2020 Classic catalogue by Weaver et al. (2022), as the best available comparison for stellar masses and SFRs. As already reported in Sect. 2,

[4] Available here: http://st-dm.pages.euclid-sgs.uk/data-product-doc/dmdr1/index.html

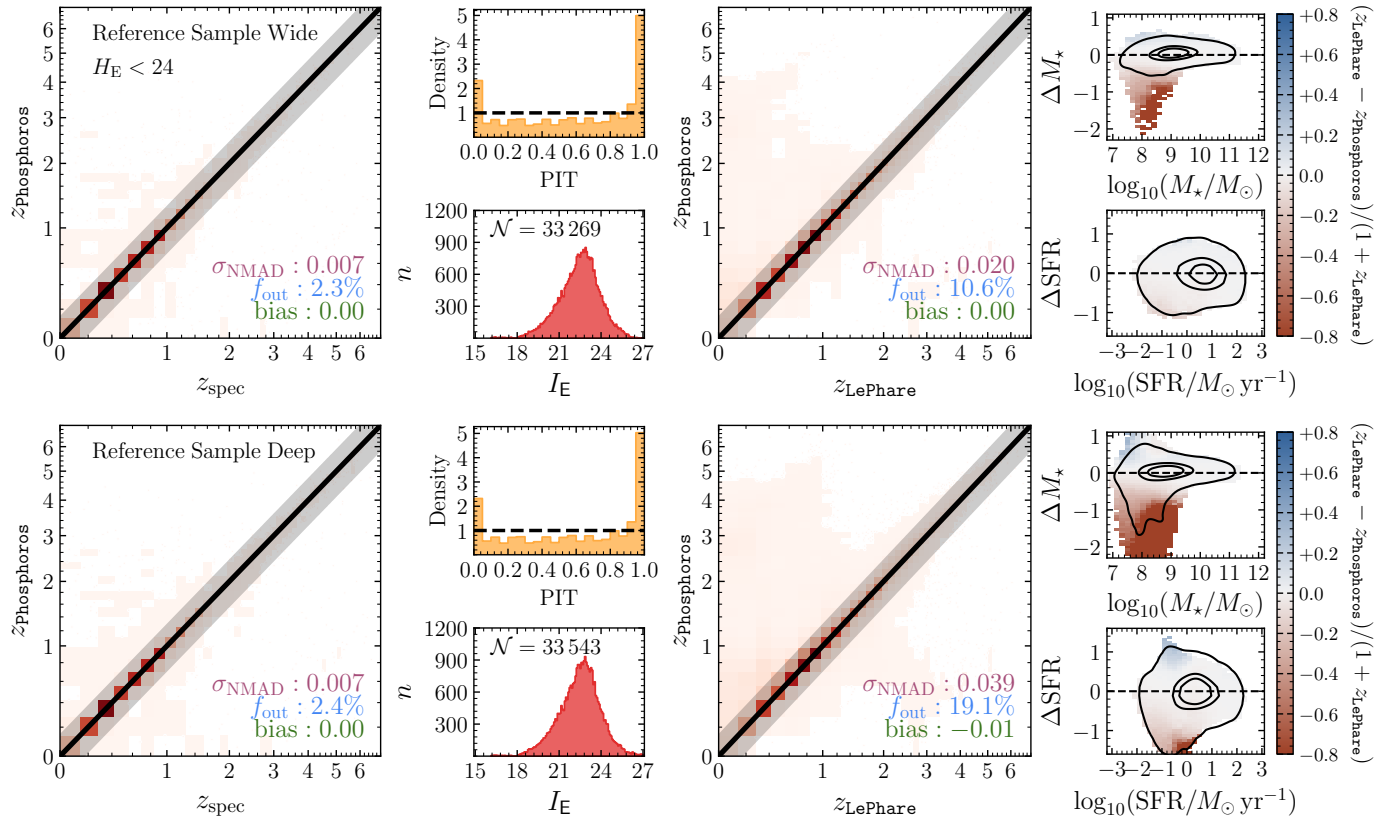


Fig. 3. Comparison between the reference sample for the EWS (first row) and EDFs (second row) used in DR1. In the first column, the comparison is made with the subsample of reference sample sources that matched with the compilation of spectroscopic redshifts in COSMOS by Khostovan et al. (2026). In the third column, the comparison is instead with the best-fit `LePhare` results for all the reference sample sources that matched with the COSMOS2020 Classic catalogue (Weaver et al. 2022). The black line is the 1:1 relation, while the shaded grey area is the region beyond which a prediction is considered to be an outlier. The reported metrics are σ_{NMAD} (purple), the outlier fraction, f_{out} (blue), and the bias (green), all defined in Sect. 4.1. The PIT (second columns) is measured as in Eq. (5) for redshifts. The fourth column shows the difference `LePhare` minus `Phosphoros` photometric redshifts, normalized to the `LePhare` photo-zs, while ΔM_* is the difference between the `LePhare` and `Phosphoros` best-fit measured logarithmic masses (see Sect. 3 for further details), and similarly for SFRs. The contours are the area containing 86%, 39% (corresponding to the 2σ and 1σ levels for a 2D histogram), and 20% of the sample.

we selected only sources with redshift quality $Q_f = 4$. We caution that the spectroscopic samples used for validation are not representative of the full photometric sample: this quality flag cut preferentially retains secure redshifts for bright sources or sources with a high S/N, for which photometric redshift recovery is more reliable. Thus, the reported σ_{NMAD} and outlier fractions are likely mild underestimates of the true values for the full survey population, particularly at the faint end. This effect is reported in Table 4, where the degradation of performance with increasing I_E magnitude is evident.

The results are presented in Fig. 3. In the top panels, we report the results for the reference sample for the EWS; in the bottom panel, the one for the EDFs. The leftmost panels always report the comparison between the `Phosphoros`-recovered photometric redshifts and the spectroscopic ones, with 33 269 matches for the EWS and 33 543 for the EDFs. In both cases, the metrics are almost the same – namely $\sigma_{NMAD} = 0.007$, outlier fraction around 2.3%, no bias – with an almost negligible difference of 0.1% in the outlier fraction between the EWS and the EDFs, a consequence of the magnitude cut removing a small fraction (about 200) of the fainter objects with an incorrect redshift attribution. The PIT distributions, shown in the centre left panel of Fig. 3, are broadly flat for both fields, indicating that the photometric redshift PDFs are well-calibrated, with no significant signs of over or underestimation of the width of the PDFs, and only a mild excess at the edges of the distribution tracing the small fraction of catastrophic outliers already captured by f_{out}.

In the right panels, we show a direct comparison with the COSMOS2020 catalogue, specifically the `LePhare` redshifts, where both axes show photo-zs estimates. The difference between EWS and EDFs is expected, given the magnitude cut at $H_E < 24$ for the former, which reduces the number of objects almost by half from 628 281 to 374 829, removing mostly fainter galaxies, which are more difficult to place in redshift. The rightmost panels highlight the difference between the `LePhare`'s estimated stellar masses and SFRs and the same quantities in the reference sample (there called ΔM_* and ΔSFR), colour-coded per the median normalised redshift difference in the bin $(z_{spec} - z_{phot})/(1 + z_{spec})$. As the contours show, the vast majority ($> 95\%$) of the reference sample has stellar masses and SFRs in good accordance with the ones from the COSMOS2020 catalogue, within 0.2–0.4 dex for the stellar masses and 1 dex for SFRs. These checks assure us about the quality of the reference sample and its use in recovering the photo-zs and PPs for the *Euclid* non-cosmological science results.

As a first test of the pipeline results, we compared them with observations of the EAFs, in particular the innermost part of COSMOS (called the Performance Verification Phase 5 field, or PV-005) and the CDFS (a sub-field within the EDF-F). These fields have been observed multiple times, more than the EWS

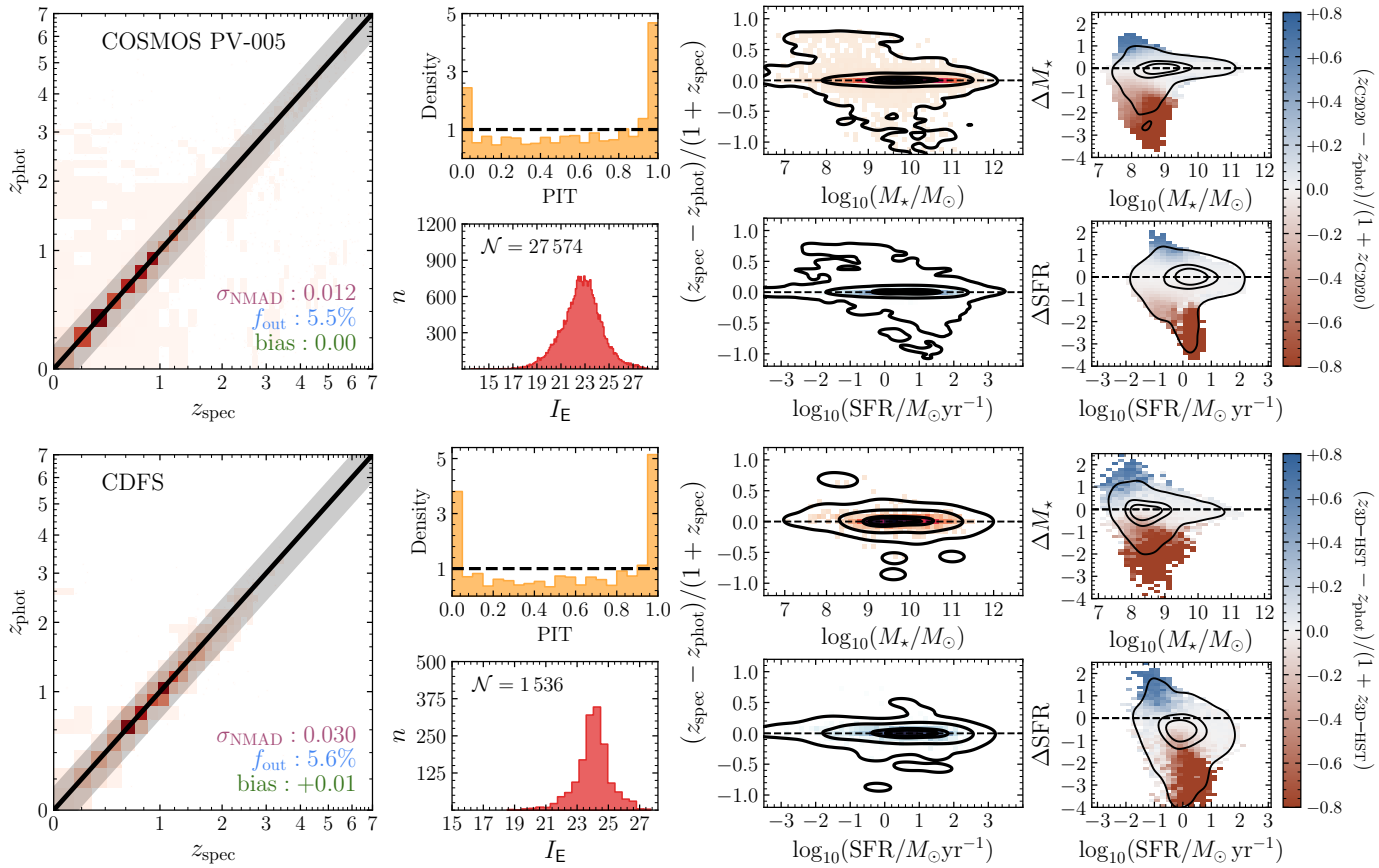


Fig. 4. Results for the COSMOS PV-005 (first row) and CDFS (second row), two of the EAFs. *First column*: comparison between the PHZ-PP measured photometric redshifts, and the compilation of spectroscopic redshifts in Khostovan et al. (2026) for COSMOS, and Brammer et al. (2012) for CDFS, with associated distribution of $I_{\rm E}$ magnitudes (second column, bottom). Other plots and lines as in Fig. 3. *Fourth column*: the difference between the `LePhare` best-fit measured masses in the COSMOS2020 Classic catalogue (first row) and one in 3D-HST (second row), and the `NNPZ` measured stellar masses, defined as ΔM_*; similar for SFR. Everything is colour coded per the normalized difference between the parent catalogue (best) photometric redshift, and the *Euclid* PHZ one. Contours are the same as in Fig. 3.

or EDFs (see Table 1), which should result in better recovered photo-zs and PPs. In both cases we used ancillary data to quantify the goodness of the pipeline results, i.e., the previously reported COSMOS2020 catalogues (Weaver et al. 2022; Khostovan et al. 2026) and the 3D-HST ones (van Dokkum et al. 2013; Momcheva et al. 2016). As the main focus of this work are galaxies, we further cleaned the samples by removing those sources flagged as X-ray detected.

The results are reported in Fig. 4. For these fields, we also applied the photometric, classification, and quality cuts reported in Sect. 2. We once again find reassuring results, with $\sigma_{\rm NMAD}$ of 0.012 (PV-005, on 27 574 galaxies with spec-z) and 0.03 (CDFS, on 1536 galaxies with spec-z), and small outlier fractions of 5.5% and 5.6%. The small bias of +0.01 in the CDFS is probably just a statistical fluctuation due to the small number and distribution of spec-z objects. The centre-right panels show, for the spec-z subsamples, the normalised redshift difference as a function of the distribution of stellar masses and SFRs. For Q1, as a consequence of the specifics of the method to infer results for non-cosmological science, similar plots showed how the non-negligible fraction of objects with unrealistically high SFRs ($10^{3-4}\,M_\odot\,\mathrm{yr}^{-1}$) were all due to a wrong redshift attribution (see e.g. Figure 3 of Euclid Collaboration: Enia et al. 2026). In the new results, the impact of these outliers is limited, if not absent (the log-normal scaling factor in `NNPZ` reduces the chances of finding such extreme objects), and the resulting PPs are indeed better constrained and occupy a more reasonable region of the PPs space.

4.3. Euclid Wide Survey

While the EWS covers the vast majority of the *Euclid* observed extragalactic sky, most of the inference regarding the quality of the data products comes from the EWS-like processing of the fields with the most ancillary data for comparison, i.e., the EDF-N for the Northern hemisphere (EWS-N), and the EDF-F for the Southern hemisphere (EWS-S). The EDFs are obtained by stacking multiple ROSs on the same field (see Sect. 2, and also Euclid Collaboration: Aussel et al. 2026; Euclid Collaboration: Kümmel et al. 2026); each single pass on the EDFs is effectively the same as an EWS pass (thus EWS-like processing). Therefore, we inferred the quality of the data products for the EWS by looking at the data quality of the single EWS-like processing of the EDF-F and EDF-N.

The results are shown in Fig. 5. The leftmost, centre-left, and centre panels are for the EWS-N, while the centre-right and rightmost panel are for EWS-S. The recovered photometric redshifts, in accord with the ones from the cosmological pipeline (Euclid Collaboration: Hartley et al. 2026), show an important improvement with respect to the ones reported in Q1 (Euclid Collaboration: Tucci et al. 2026) – $\sigma_{\rm NMAD}$ decreasing from about 0.03 to 0.02, and around 10% fewer catastrophic outliers – where

Table 4. The quality of the recovered photo-zs in the PHZ-PP pipeline, overall and in bins of I_E magnitude.

Field	Metric	All	$15 < I_E \leq 21.5$	$21.5 < I_E \leq 23$	$23 < I_E \leq 25$
EDF-N	$\mathcal{N}$	19 291	9510	5884	3756
	$\sigma_{\rm NMAD}$	0.022	0.023	0.018	0.023
	$f_{\rm out}$ (%)	2.8	1.6	2.5	5.5
	bias	0.00	0.00	0.00	0.00
EDF-S	$\mathcal{N}$	74	49	25	0
	$\sigma_{\rm NMAD}$	0.023	0.020	0.027	...
	$f_{\rm out}$ (%)	6.8	6.1	8.0	...
	bias	+0.01	+0.01	+0.01	...
EDF-F	$\mathcal{N}$	52 582	23 790	20 966	6274
	$\sigma_{\rm NMAD}$	0.025	0.025	0.024	0.036
	$f_{\rm out}$ (%)	8.0	5.6	7.6	14.2
	bias	0.00	0.00	0.00	0.00
CDFS	$\mathcal{N}$	1536	43	182	1097
	$\sigma_{\rm NMAD}$	0.030	0.016	0.016	0.030
	$f_{\rm out}$ (%)	5.6	0.0	2.7	5.4
	bias	+0.01	0.00	+0.01	+0.01
COSMOS PV-005	$\mathcal{N}$	27 574	6013	9823	10 186
	$\sigma_{\rm NMAD}$	0.012	0.010	0.009	0.015
	$f_{\rm out}$ (%)	5.5	1.8	2.6	6.6
	bias	0.00	0.00	0.00	0.00
EWS-N	$\mathcal{N}$	19 291	9510	5884	3756
	$\sigma_{\rm NMAD}$	0.021	0.017	0.022	0.034
	$f_{\rm out}$ (%)	3.7	0.4	3.8	9.4
	bias	+0.01	+0.01	+0.01	0.00
EWS-S	$\mathcal{N}$	52 582	23 790	20 966	6274
	$\sigma_{\rm NMAD}$	0.027	0.024	0.025	0.048
	$f_{\rm out}$ (%)	7.6	4.4	7.2	16.2
	bias	0.00	0.00	+0.01	0.00

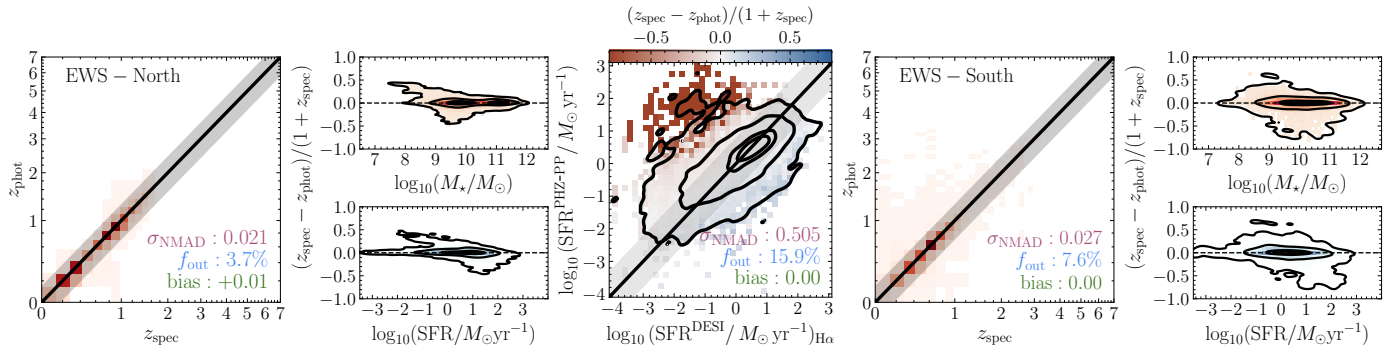


Fig. 5. Results for the EWS-like processing of EDF-N (first, second, and third column), which can be considered as a proxy for the EWS in the northern hemisphere, and EDF-F (fourth and fifth column), which can be considered as a proxy for the EWS in the southern hemisphere. Contours are similar to those in Fig. 3.

the impossibility of building a reference sample from observations of true galaxies forced the use of a reference sample of synthetic models built from BC03 galaxies, with some issues especially in the recovery of the specific SFRs (see Section 6.1.1 of Euclid Collaboration: Tucci et al. 2026).

Other than the available compilations of spectroscopic redshifts, we also compared the PHZ inferred SFRs with the ones coming from multiple observations of both Hα and Hβ emission lines in DESI. These are available only for a limited number (around 3000) of sources in the EWS-N, but are the best available measurements to compare the SFRs to, and hence the closest possible ground truth values for this PPs. Accounting for how the SFRs were estimated – that is, from broad-band photometry extending to 1.6 µm in the observed-frame – the results are as expected. As reported in the centre panel of Fig. 5, a $\sigma_{\rm NMAD}$ of 0.505 and an outlier fraction of 16% (and no bias) are actually less than what was expected from numerical simulations (Euclid Collaboration: Enia et al. 2024). The observed scatter with respect to the 1:1 relation is inherent due to the difficulties of inferring SFRs from the photometric data only and not just a consequence of a wrong redshift measurement; however, wrongly measured redshifts populate the vast majority of the catastrophic outliers found outside of a 0.8 dex cushion, especially from lower-z galaxies misplaced to higher-z.

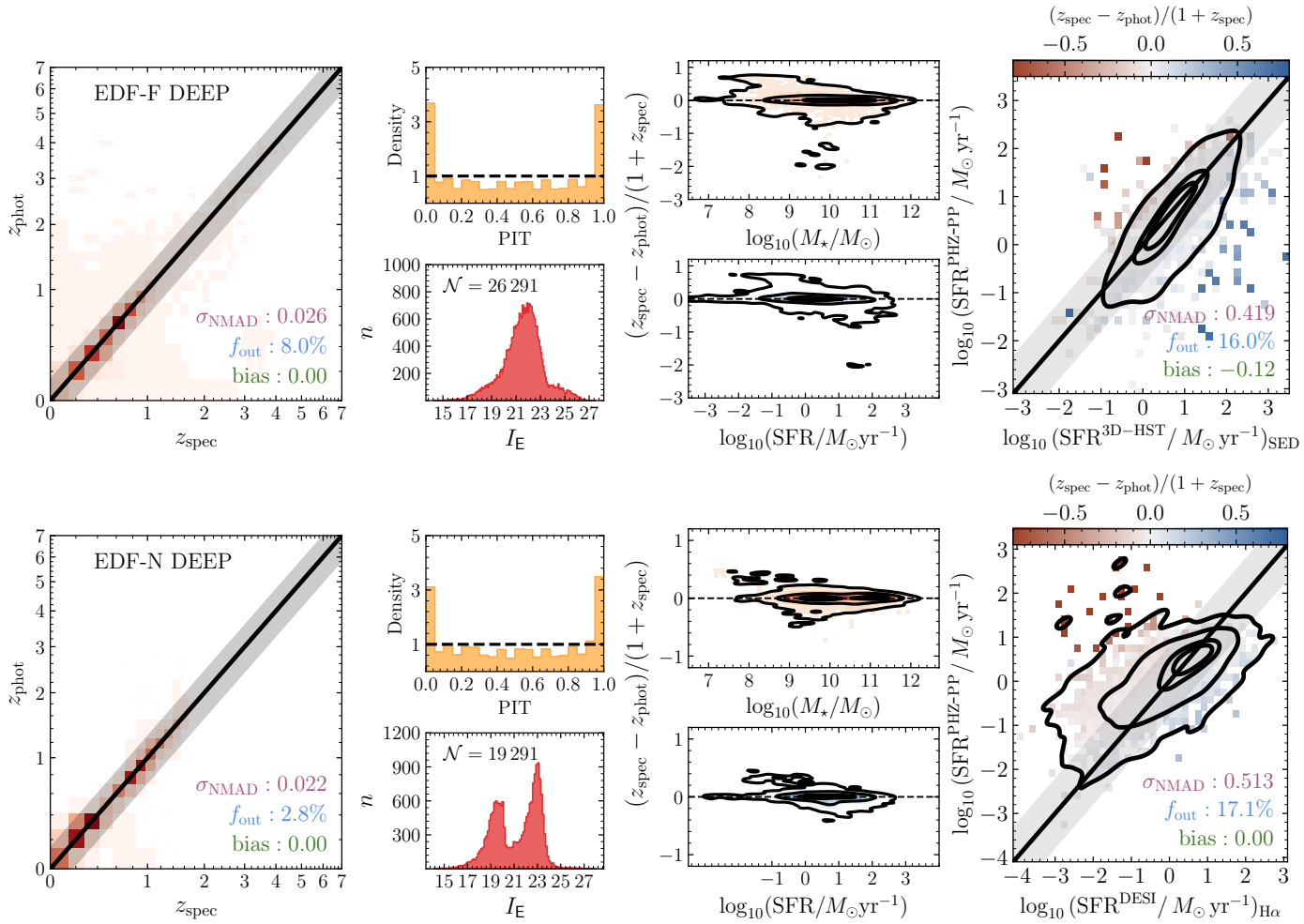


Fig. 6. Results for the Deep processing of EDF-F (*top panels*) and EDF-N (*bottom panels*). *Left*: comparison between the PHZ-PP measured photometric redshifts, and a compilation of spectroscopic redshifts (see Sect. 2). Other plots and lines as in Fig. 3. *Right*: like the centre panel of Fig. 5; for EDF-F the comparison is with the SED-fitting inferred SFR in GOODS-S in 3D-HST; for EDF-N, with the H α and Hβ detected lines in DESI.

4.4. Euclid Deep Fields

There are three fields that compose the EDFs: the EDF-N (20 deg^2), near the Northern Ecliptic Pole; the EDF-F (10 deg^2), in the Fornax cluster which has been the subject of multiple multi-wavelength surveys in the past (e.g., GOODS-S); the EDF-S (20 deg^2), in an area of the Southern sky where the Galactic extinction is at its lowest level. While the plan is to observe all of them with (at least) 40 ROSs, for DR1 there are eleven ROSs for EDF-N and ten for the EDF-S, and two ROSs for EDF-F.

As reported in Sect. 4.3, we used a compilation of ancillary data to infer the quality of the data products. The results are reported in Fig. 6. The depth improvement with respect to the EWS is reflected in the quality of the recovered photo-zs. For EDF-N, we find $\sigma_{\rm NMAD}$ = 0.022 and an outlier fraction of 2.8%, with no bias, using a spectroscopic sample of 19 291 galaxies. Since EDF-F has been observed fewer times, the results are understandably poorer, with $\sigma_{\rm NMAD}$ = 0.026 and an outlier fraction of 8.0%, for a larger spectroscopic sample of 52 582 galaxies; this is consistent with what is found for the EWS-like processing of the same field (see Sect. 4.3) and reflects the larger diversity of galaxy types and redshift distributions sampled by the deeper observations, as well as the higher fraction of faint sources included in the spectroscopic comparison sample. For EDF-S, the very limited number of available spectroscopic redshifts (74 in total, with none fainter than $I_{\rm E}$ = 23, as reported in Sect. 2) prevents a thorough assessment of the pipeline performance; the metrics we recover – $\sigma_{\rm NMAD}$ = 0.023, $f_{\rm out}$ = 6.8%, and a positive bias of +0.01, almost negligible given the small number of spectroscopic redshifts available – are nevertheless consistent with what is found for the other two EDFs. In all three fields, the PIT distributions are broadly flat, indicating well-calibrated photo-z PDFs, with only minor signs of a slight overestimation of the PDF widths.

As in Sect. 4.3, we complemented the photo-z validation with a comparison of the PHZ-inferred SFRs against external estimates. For EDF-F, we used the SED-fitting inferred SFRs from the 3D-HST catalogue in GOODS-S (Momcheva et al. 2016), while for EDF-N, we used the H α and Hβ-based SFRs from the DESI value-added catalogue (Siudek et al. 2024). The results are shown in the rightmost panels of Fig. 6. For EDF-F, we find $\sigma_{\rm NMAD}$ = 0.419 and an outlier fraction of 16.0%, with a small negative bias of −0.12 dex with respect to the 3D-HST SED-fitting SFRs, while for EDF-N we find $\sigma_{\rm NMAD}$ = 0.513, outlier fraction of 17.1%, and a bias b = 0 with respect to the DESI H α measurements. These numbers are consistent with what is found for the EWS-like processing (Fig. 5), confirming that the dominant source of scatter in the recovered SFRs is the intrinsic

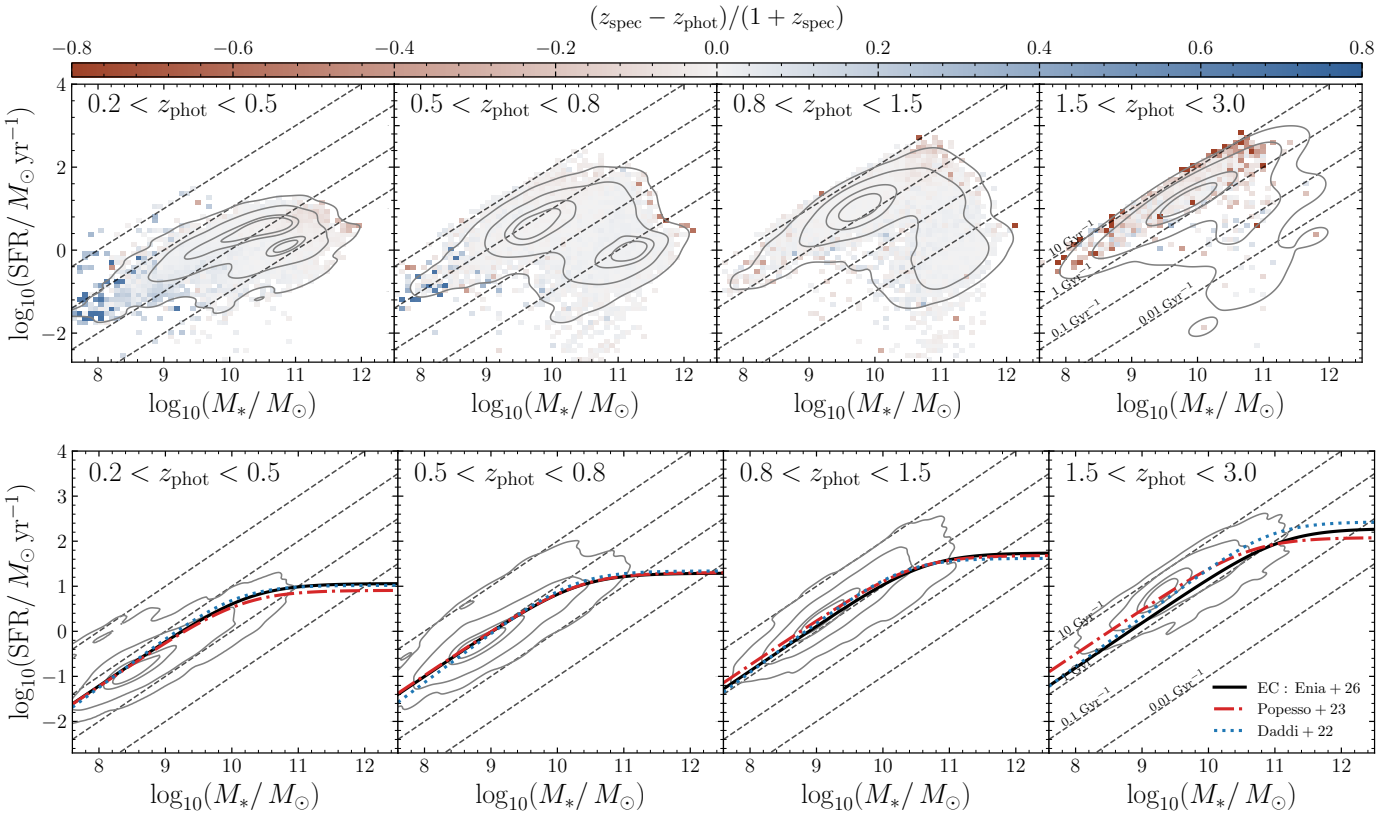


Fig. 7. Insight into the SFMS in the EDFs. *Top*: SFR–M_* relation for the sample with available spectroscopic redshifts, colour-coded by the normalised redshift difference, in four different redshift bins. Blue squares highlight redshift underestimations, and the opposite for the red ones. *Bottom*: SFR–M_* plot, compared with a compilation of published SFMS determnations from Euclid Collaboration: Enia et al. (2026, dashed black line), Popesso et al. (2023, dashed-dotted red line), and Daddi et al. (2022, dotted blue line), all evaluated at the median redshift of each redshift bin (or to the closest reported value). Dashed grey lines highlight loci of constant sSFR.

difficulty of inferring this quantity from broad-band photometry alone, rather than a systematic effect introduced by the depth of the observations or the specific ancillary data set used for comparison. As already noted for the EWS, the catastrophic outliers in the SFR comparison are predominantly associated with catastrophic failures in the photometric redshift recovery, with low-z galaxies misplaced at higher redshift artificially boosting their inferred SFRs. We note that a complementary view of the *Euclid*-inferred SFRs could be provided by the statistical comparison with far-infrared photometry from *Herschel* and SCUBA-2 via stacking, as done in Euclid Collaboration: Hill et al. (2026), which finds broadly consistent SFRs with respect to the *Euclid*-inferred ones for SFMS galaxies in Q1.

For the sub-sample of sources with available spectroscopic redshifts, we tested the quality of the recovered PPs across different regions of the M_*–SFR plane as a function of the normalised redshift residual, in four redshift bins. We then extended the analysis to all sources in the EDFs satisfying the quality cuts of Sect. 2, comparing their distribution in the M_*–SFR plane with different published functional forms of the SFMS. In both cases, we split the data into four redshift bins: [0.2, 0.5], [0.5, 0.8], [0.8, 1.5], [1.5, 3.0]. In the top panels of Fig. 7, we report the median distribution of spec-z galaxies in bins within the M_*–SFR plane, coloured by their normalised redshift distribution $(z_{\rm spec} - z_{\rm phot})/(1 + z_{\rm spec})$. Ideally, when the colours start to diverge from white it means that the median normalised spectroscopic redshift difference in the bin is that of a catastrophic outlier (see definition in Sect. 4). Red values indicate a redshift over-estimation, while blue values the opposite. The contours contain the area with 90%, 86%, 39% (corresponding to the 3 σ, 2 σ, and 1 σ levels for a 2D histogram), and 20% of the sample. Thanks to the deeper data and especially the different definition of the reference sample and the scaling in `NNPZ`, the DR1 results show an important improvement with respect to the Q1 results, even in the case when the first two IRAC channels were added (as visible in Figure 4 in Euclid Collaboration: Enia et al. 2026). Where the majority of the (spectroscopic) sample lies, the quality of the recovered photometric redshift is extremely good, out to $z \sim 1.5$, still good out to $z \sim 3$, and with the signs of a (moderately) wrong redshift attribution only for high sSFRs.

In the lower panels, we show the M_*–SFR plane for the sample of SFGs selected with the UVJ colours, in terms of contours highlighting the number density of the full sample of SFGs in DR1. There, we report three previously published SFMS relations for comparison: Eq. (15) of Popesso et al. (2023, red dashed-dotted line), that is, a comprehensive compilation of 27 SFMS relations from the literature fitted to the same functional form, in the mass range $8.5 < \log_{10}(M_*/M_\odot) < 11.5$; Daddi et al. (2022, dotted blue line), obtained from a stacking analysis of about 400 000 colour-selected SFGs in COSMOS (Delvecchio et al. 2021), here also in the mass range $8.5 < \log_{10}(M_*/M_\odot) < 11.5$; and Euclid Collaboration: Enia et al. (2026, black solid line), a fit of the SFMS on the first Euclid Q1 data release, for more than eight million sources in the mass range $8.0 < \log_{10}(M_*/M_\odot) < 11.5$, and about 35 000 in the highest mass bin, which better constrains the bending of the SFMS. We observe reasonable agreement between the SFMS functional forms and the data, especially in the intermediate, more reliable

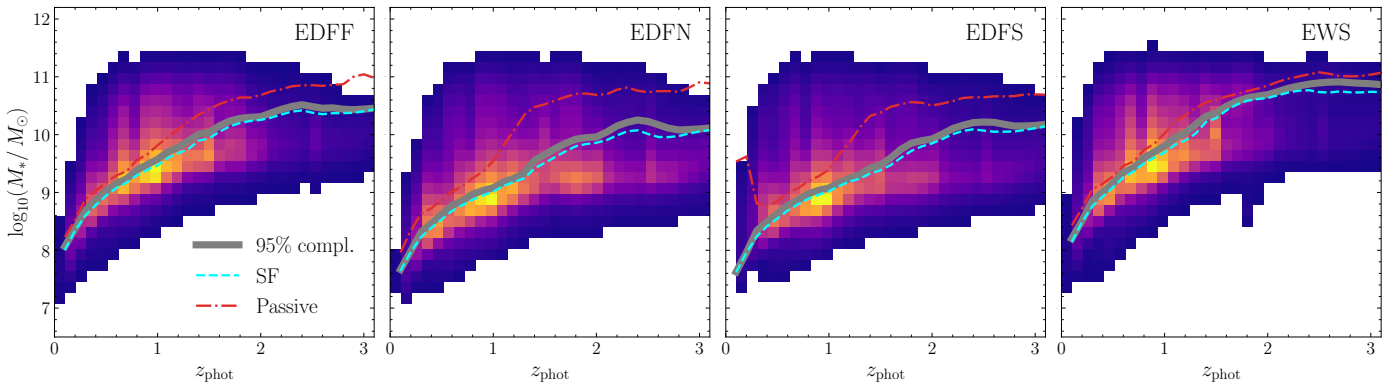


Fig. 8. Stellar mass completeness for the DR1 (Pozzetti et al. 2010), cut at each field depth in $H_{\rm E}$ (Table 1), shown as the density of galaxies in the photometric redshifts versus stellar mass plane. The solid grey line is the 95% stellar mass completeness limit, the red dashed-dotted line for passive galaxies, and the cyan dashed line for star-forming galaxies (SFGs).

redshift bins; going to higher redshifts, the DR1 results are a few dex ($\sim$ 0.1–0.2) higher with respect to the SFMS in Daddi et al. (2022) and Euclid Collaboration: Enia et al. (2026), and slightly more in accord with the one in Popesso et al. (2023).

4.5. Stellar mass completeness

In order to estimate the mass completeness of the DR1, we followed the method described in Pozzetti et al. (2010). We selected galaxies close to the limiting $H_{\rm E}$ magnitude of each field, measured for each galaxy the mass they would have at the limiting magnitude as

$$\log_{10}(M_{\rm lim}/M_\odot) = \log_{10}(M_*/M_\odot) + 0.4(H_{\rm E} - H_{\rm E,lim})\,. \quad (6)$$

The 95th percentile of the distribution of $M_{\rm lim}(z)$ for each redshift bin is the mass completeness, reported in Fig. 8 as grey lines. The classification into star-forming (dashed blue line) and passive galaxies (dash-dotted red line) was performed with the selection criteria based on the UVJ colours (Labbé et al. 2005; Wuyts et al. 2007; Williams et al. 2010), but updated to the *Euclid* rest-frame colours (Euclid Consortium: Mao et al. in prep.). Given the different field depths and multiwavelength coverage, we report the mass completeness separately for each field. The trend is broadly similar across all the EDFs – with EDF-F having higher values by $\sim$ 0.25 dex – with the 95% completeness limit rising from $\log_{10}(M_*/M_\odot) \sim 8$ at $z \sim 0.1$ to $\sim$ 9.0–9.3 at $z \sim 1$, and further increasing to $\log_{10}(M_*/M_\odot) \sim$ 10–10.3 at $z \sim$ 2.5–3. The completeness limit for passive galaxies is $\sim$ 0.4–0.6 dex higher than for star-forming ones at all redshifts, a consequence of their redder colours and higher mass-to-light ratios at fixed magnitude. A similar trend is observed for EWS, although with higher values. We also checked if there were any differences between the EWS-S and EWS-N and found none. Finally, as a rule-of-thumb, rescaling the whole mass completeness to a less conservative 5 σ limit – which might be more appropriate depending on the scientific case – means shifting the curves towards lower masses by (0.30$\pm$0.02) dex, if considering a $\pm$0.05 variation in the limiting magnitudes.

5. Conclusions

We have described the PHZ pipeline for the *Euclid* DR1, in particular the non-cosmological science branch responsible for recovering photo-zs and PPs of galaxies. The pipeline is built around the nearest-neighbour algorithm `NNPZ`, which, for DR1, benefits from a fundamentally improved reference sample with respect to Q1: rather than relying on a grid of synthetic BC03 templates, the reference sample is now anchored to real *Euclid* observations of galaxies in the COSMOS field, matched to the COSMOS2020 catalogue and labelled through a dedicated `Phosphoros` run. This approach ensures internal consistency between the core-science and non-cosmological science branches of the PHZ pipeline, since the photometric redshift probability distribution functions from the core-science run are directly propagated into the construction of the PP labels.

We constructed two versions of the reference sample – one for the EWS (approximately 375 000 galaxies, cut at $H_{\rm E} < 24$) and one for the EDFs (630 000 galaxies, with no magnitude cut) – and introduced a set of additional measures to mitigate the risk of overfitting the sample variance of COSMOS and the occurrence of unphysical outliers in the recovered stellar masses, namely a source-weighting scheme and a lognormal prior on the SED amplitude scaling factor. The data products released through the pipeline cover the full extent of the DR1 footprint – the EWS, the three EDFs, and the EAFs – and include photo-zs, stellar masses, SFRs, and other properties reported in Table 3, alongside their associated PDFs (Table 2).

The validation results confirm the quality of the DR1 data products across all fields and processing depths. The reference sample itself shows excellent agreement with available spectroscopic redshifts, with $\sigma_{\rm NMAD} = 0.007$ and an outlier fraction of 2.3%, comparable to or slightly better than the state-of-the-art results from the COSMOS2020 catalogue. For the EAFs – in particular the PV-005 observations of COSMOS and CDFS – both observed more times than the EWS and reaching depths of $I_{\rm E} \sim$ 26.2 and 26.4, respectively (Table 1) – $\sigma_{\rm NMAD}$ of 0.012 and 0.030 are obtained respectively, with small outlier fractions and negligible biases, on spectroscopic samples of 28 118 and 1536 galaxies reaching down to $I_{\rm E} \sim$ 25–27. For the EWS, inferred from the EWS-like processing of the EDF-N and EDF-F (reaching $I_{\rm E} \sim$ 26.2 and 24.9, respectively, but processed at EWS depth of $I_{\rm E} \sim$ 24.8), $\sigma_{\rm NMAD}$ of 0.021 (North) and 0.027 (South) are obtained, with outlier fractions of 3.7% and 7.6% – a significant improvement with respect to the Q1 results (where $\sigma_{\rm NMAD}$ of around 0.03 were reported), driven by the use of a real-galaxy reference sample. For the EDFs, despite being deeper than the EWS (at least for the EDF-N with $I_{\rm E} \sim$ 26.2, while the EDF-F is more similar at 24.9, compared to $\sim$ 24.8 for the EWS), the spectroscopic comparison samples are correspondingly fainter, probing a more diverse and challenging galaxy population; the

results are nevertheless consistent with the EWS findings, with $\sigma_{\rm NMAD}$ of 0.022 and 0.025 for EDF-N and EDF-F respectively. The comparison of SFRs with DESI Hα and Hβ measurements yields a $\sigma_{\rm NMAD}$ of $\sim$ 0.5 dex and outlier fractions of $\sim$ 16%, results that are in line with expectations from numerical simulations and reflect the inherent difficulty of inferring SFRs from broad-band photometry alone. Finally, the distribution of SFGs in the M_*–SFR plane across the EDFs is shown to be in good agreement with well-known SFMS relations, further confirming the overall reliability of the recovered PPs.

Euclid DR1 constitutes a major step forward for extragalactic astrophysics, with nearly 880 million detected sources across more than 1900 deg^2 of the extragalactic sky, and reliable photo-zs and PPs derived from a self-consistent, observation-based pipeline. It represents the largest homogeneous catalogue of galaxy physical properties ever assembled. Future data releases, benefiting from an ever-growing survey footprint, deeper observations of the EDFs, and continued improvements to the reference sample and the NNPZ pipeline, will further extend and refine these results, solidifying *Euclid*'s role as a cornerstone resource for the study of galaxy formation and evolution.

Acknowledgements. AnEn, MiBo, LuPo, SoFo, ViAl, MaMe, SaQu, DaVe, MaTa, acknowledge support from the ELSA project. "ELSA: Euclid Legacy Science Advanced analysis tools" (Grant Agreement no. 101135203) is funded by the European Union. Views and opinions expressed are however those of the author(s) only and do not necessarily reflect those of the European Union or Innovate UK. Neither the European Union nor the granting authority can be held responsible for them. UK participation is funded through the UK HORIZON guarantee scheme under Innovate UK grant 10093177. MiBo, AnEn acknowledge the support from INAF Minigrant 2023 'ADIEU'. This research makes use of ESA Datalabs (datalabs.esa.int), an initiative by ESA's Data Science and Archives Division in the Science and Operations Department, Directorate of Science. The Euclid Consortium acknowledges the European Space Agency and a number of agencies and institutes that have supported the development of *Euclid*, in particular the Agenzia Spaziale Italiana, the Austrian Forschungsförderungsgesellschaft funded through BMIMI, the Belgian Science Policy, the Canadian Euclid Consortium, the Deutsches Zentrum für Luft- und Raumfahrt, the DTU Space and the Niels Bohr Institute in Denmark, the French Centre National d'Etudes Spatiales, the Fundação para a Ciência e a Tecnologia, the Hungarian Academy of Sciences, the Ministerio de Ciencia, Innovación y Universidades, the National Aeronautics and Space Administration, the National Astronomical Observatory of Japan, the Netherlandse Onderzoekschool Voor Astronomie, the Norwegian Space Agency, the Research Council of Finland, the Romanian Space Agency, the Swiss Space Office (SSO) at the State Secretariat for Education, Research, and Innovation (SERI), and the United Kingdom Space Agency. A complete and detailed list is available on the *Euclid* web site (www.euclid-ec.org/consortium/community/). This work has made use of the Euclid Data Release 1 (DR1) from the European Space Agency (ESA) mission *Euclid*, available at https://www.cosmos.esa.int/web/euclid/data-release-dr1.

References

Brammer, G. B., Sánchez-Janssen, R., Labbé, I., et al. 2012, ApJ, 758, L17
Bruzual, G. & Charlot, S. 2003, MNRAS, 344, 1000
Chabrier, G. 2003, PASP, 115, 763
Daddi, E., Delvecchio, I., Dimauro, P., et al. 2022, A&A, 661, L7
Dawid, A. P. 1984, Royal Statistical Society. Journal. Series A: General, 147, 278
Delvecchio, I., Daddi, E., Sargent, M. T., et al. 2021, A&A, 647, A123
DES Collaboration: Abbott, T., Abdalla, F. B., Aleksić, J., et al. 2016, MNRAS, 460, 1270
DESI Collaboration: Aghamousa, A., Aguilar, J., Ahlen, S., et al. 2016, arXiv:1611.00036
D'Isanto, A. & Polsterer, K. L. 2018, A&A, 609, A111
Euclid Collaboration: Aussel, H. et al. 2026, arXiv, submitted
Euclid Collaboration: Corcho-Caballero, P., Balbinot, E., De Jong, J., et al. 2026, A&A, submitted
Euclid Collaboration: Cropper, M., Al-Bahlawan, A., Amiaux, J., et al. 2025, A&A, 697, A2
Euclid Collaboration: Desprez, G., Paltani, S., Coupon, J., et al. 2020, A&A, 644, A31
Euclid Collaboration: Enia, A., Bolzonella, M., Pozzetti, L., et al. 2024, A&A, 691, A175
Euclid Collaboration: Enia, A., Pozzetti, L., Bolzonella, M., et al. 2026, A&A, 711, A14
Euclid Collaboration: Fumana, M., Copin, Y., Appleton, P., et al. 2026, A&A, submitted
Euclid Collaboration: Gasparetto, T., Merlin, E., Castellano, M., et al. 2026, A&A, submitted
Euclid Collaboration: Hartley, W., Paltani, S., Dubath, F., et al. 2026, A&A, submitted
Euclid Collaboration: Hill, R., Abghari, A., Scott, D., et al. 2026, A&A, 711, A23
Euclid Collaboration: Jahnke, K., Gillard, W., Schirmer, M., et al. 2025, A&A, 697, A3
Euclid Collaboration: Kümmel, M., Caro, F., Dimauro, P., et al. 2026, A&A, submitted
Euclid Collaboration: McCracken, H., Benson, K., Cropper, M., et al. 2026, A&A, submitted
Euclid Collaboration: McPartland, C. J. R., Zalesky, L., Weaver, J. R., et al. 2025, A&A, 695, A259
Euclid Collaboration: Mellier, Y., Abdurro'uf, Acevedo Barroso, J., et al. 2025, A&A, 697, A1
Euclid Collaboration: Odier, J., Macias-Perez, J., Alguero, G., et al. 2026, arXiv, submitted
Euclid Collaboration: Polenta, G., Frailis, M., Alavi, A., et al. 2026, A&A, submitted
Euclid Collaboration: Scaramella, R., Amiaux, J., Mellier, Y., et al. 2022, A&A, 662, A112
Euclid Collaboration: Scodeggio, M., Copin, Y., et al. 2026, in preparation
Euclid Collaboration: Tereno, I., Dinis, J., Dupac, X., et al. 2026, arXiv, submitted
Euclid Collaboration: Tucci, M., Paltani, S., Hartley, W. G., et al. 2026, A&A, 711, A5
Euclid Data Release 1. 2026, https://doi.org/10.57780/esa-d079c51
Flaugher, B., Diehl, H. T., Honscheid, K., et al. 2015, AJ, 150, 150
Gwyn, S., McConnachie, A. W., Cuillandre, J.-C., et al. 2025, AJ, 170, 324
Ivezic, Z., Axelrod, T., Brandt, W. N., et al. 2008, Serbian Astron. J., 176, 1
Kennicutt, Robert C., J. 1998, ApJ, 498, 541
Khostovan, A. A., Kartaltepe, J. S., Salvato, M., et al. 2026, ApJS, 282, 6
Labbé, I., Huang, J., Franx, M., et al. 2005, ApJ, 624, L81
Merlin, E., Bourne, N., Castellano, M., et al. 2016, A&A, 595, A97
Merlin, E., Fontana, A., Ferguson, H. C., et al. 2015, A&A, 582, A15
Momcheva, I. G., Brammer, G. B., van Dokkum, P. G., et al. 2016, ApJS, 225, 27
Oke, J. B. & Gunn, J. E. 1983, ApJ, 266, 713
Planck Collaboration, Ade, P. A. R., Aghanim, N., et al. 2016, A&A, 594, A13
Popesso, P., Concas, A., Cresci, G., et al. 2023, MNRAS, 519, 1526
Pozzetti, L., Bolzonella, M., Zucca, E., et al. 2010, A&A, 523, A13
Siudek, M., Pucha, R., Mezcua, M., et al. 2024, A&A, 691, A308
Tanaka, M., Coupon, J., Hsieh, B.-C., et al. 2018, PASJ, 70, S9
van Dokkum, P., Brammer, G., Momcheva, I., Skelton, R. E., & Whitaker, K. E. 2013, arXiv:1305.2140
Weaver, J. R., Kauffmann, O. B., Ilbert, O., et al. 2022, ApJS, 258, 11
Williams, R. J., Quadri, R. F., Franx, M., et al. 2010, ApJ, 713, 738
Wuyts, S., Labbé, I., Franx, M., et al. 2007, ApJ, 655, 51

Authors and affiliations

Euclid Collaboration: A. Enia[1,2⋆], W. G. Hartley[3], M. Bolzonella[2], F. Dubath[3], S. Paltani[3], L. Pozzetti[2], C. Saulder[4,5], M. Tucci[3], N. Morisset[3], D. Scott[6], M. Salvato[4], H. Hildebrandt[7], J. G. Sorce[8,9], G. Zamorani[2], B. Altieri[10], A. Amara[11], S. Andreon[12], N. Auricchio[2], C. Baccigalupi[13,14,15,16], M. Baldi[17,2,18], A. Balestra[19], S. Bardelli[2], P. Battaglia[2], A. N. Belikov[20,21], A. Biviano[14,13], E. Branchini[22,23,12], M. Brescia[24,25], S. Camera[26,27,28], V. Capobianco[28], C. Carbone[29], J. Carretero[30,31], F. J. Castander[32,33], M. Castellano[34], G. Castignani[2], S. Cavuoti[25,35], K. C. Chambers[36], A. Cimatti[37], C. Colodro-Conde[38], G. Congedo[39], C. J. Conselice[40], L. Conversi[41,10], Y. Copin[42], A. Costille[43], F. Courbin[44,45,46], H. M. Courtois[47], M. Cropper[48], H. Degaudenzi[3], G. De Lucia[14], H. Dole[9], X. Dupac[10], S. Escoffier[49], M. Farina[50], R. Farinelli[2], S. Farrens[51], F. Faustini[34], S. Ferriol[42], F. Finelli[2,52], P. Fosalba[33,32], N. Fourmanoit[49], M. Frailis[14], E. Franceschi[2], M. Fumana[29], L. Gabarra[53], S. Galeotta[14], K. George[54], B. Gillis[39], C. Giocoli[2,18], J. Gracia-Carpio[4], A. Grazian[19], F. Grupp[4,5], S. Gwyn[55], S. V. H. Haugan[56], S. Hemmati[57], H. Hoekstra[58], W. Holmes[59], F. Hormuth[60], A. Hornstrup[61,62], M. Huertas-Company[38,63,64], K. Jahnke[65], M. Jhabvala[66], B. Joachimi[67], S. Kermiche[49], A. Kiessling[59], B. Kubik[42], M. Kümmel[5], M. Kunz[68], H. Kurki-Suonio[69,70], A. M. C. Le Brun[71], V. Le Brun[43], D. Le Mignant[43], P. Liebing[48], S. Ligori[28], P. B. Lilje[56], V. Lindholm[69,70], I. Lloro[72], M. Magliocchetti[50], G. Mainetti[73], D. Maino[74,29,75], O. Mansutti[14], S. Marcin[76], O. Marggraf[77], M. Martinelli[34,78], N. Martinet[43], F. Marulli[79,2,18], R. J. Massey[80], D. C. Masters[81], N. Mauri[37,18], E. Medinaceli[2], S. Mei[82,83], M. Melchior[84], M. Meneghetti[2,18], E. Merlin[19], G. Meylan[85], J. J. Mohr[54], P. Monaco[86,14,15,13], A. Mora[87], M. Moresco[79,2], C. Moretti[14,13,15], L. Moscardini[79,2,18], R. Nakajima[77], C. Neissner[88,31], S.-M. Niemi[89], C. Padilla[88], F. Pasian[14], W. J. Percival[90,91,92], V. Pettorino[89], A. Pezzotta[12], S. Pires[51], G. Polenta[93], M. Poncet[94], L. A. Popa[95], F. Raison[4], A. Renzi[96,97,2], J. Rhodes[59], G. Riccio[25], I. Risso[22,23,12], F. Rizzo[14], E. Romelli[14], M. Roncarelli[2], B. Rusholme[57], R. Saglia[5,4], Z. Sakr[98,99,100], A. G. Sánchez[4], D. Sapone[101], B. Sartoris[4,14], M. Schirmer[65], P. Schneider[77], T. Schrabback[102], M. Scodeggio[29], A. Secroun[49], E. Sihvola[103], C. Sirignano[96,97], G. Sirri[18], L. Stanco[97], P. Tallada-Crespí[30,31], A. N. Taylor[39], H. I. Teplitz[81], I. Tereno[104,105], N. Tessore[48], S. Toft[106,107], R. Toledo-Moreo[108,109], F. Torradeflot[31,30], I. Tutusaus[32,33,99], J. Valiviita[69,70], T. Vassallo[14,54], Y. Wang[57], J. Weller[5,4], A. Zacchei[14,13], F. M. Zerbi[12], I. A. Zinchenko[110], E. Zucca[2], V. Allevato[25], M. Ballardini[111,112,2], S. Borgani[86,13,14,15,113], E. Bozzo[3], C. Burigana[114,52], R. Cabanac[99], M. Calabrese[115,29], A. Cappi[116,2], F. Caro[34], T. Castro[117,14,13], D. Di Ferdinando[18], J. A. Escartin Vigo[4], G. Fabbian[9], J. García-Bellido[98], T. Gasparetto[34], V. Gautard[1], C. M. Gutierrez[38,118], A. Loureiro[119,120], J. Macias-Perez[121], C. Mancini[29], R. Maoli[122,34], R. B. Metcalf[79,2], M. Pöntinen[69], E. Sarpa[14], V. Scottez[123,124], M. Sereno[2,18], M. Tenti[18], M. Viel[13,14,16,15,113], M. Wiesmann[56], J. A. Acevedo Barroso[59], R. Adam[116], Y. Akrami[98,125], I. T. Andika[5], G. Angora[25,111], S. Anselmi[97,96,126], M. Archidiacono[74,75], G. Aricò[18], F. Atrio-Barandela[127], E. Aubourg[82,128], M. Baes[129], L. Bazzanini[111,2], D. Bertacca[96,19,97], M. Bethermin[130], F. Beutler[39], L. Bisigello[19], A. Blanchard[99], L. Blot[131,71], H. Böhringer[4,54,132], M. Bonici[90,29], M. L. Brown[40], S. Bruton[133], A. Calabro[34], B. Camacho Quevedo[13,16,14], C. S. Carvalho[105], F. Cogato[79,2], T. E. Collett[134], A. R. Cooray[135], P. Corcho-Caballero[20], B. Csizi[102], O. Cucciati[2], H. Dannerbauer[38,118], T. de Boer[36], G. Desprez[20], A. Díaz-Sánchez[136], S. Di Domizio[22,23], J. M. Diego[137], V. Duret[49], Y. Fang[5], A. Farina[12,23], A. M. N. Ferguson[39], A. Finoguenov[69], A. Fontana[34], A. Franco[138,139,140], Y. Fu[58,20], K. Ganga[82], R. Gavazzi[43,141], E. Gaztanaga[32,33,134], Z. Ghaffari[14,13], F. Giacomini[18], F. Gianotti[2], G. Gozaliasl[142,69], A. Gruppuso[2,18], M. Guidi[17,2], A. Hall[39], N. A. Hatch[143], C. Hernández-Monteagudo[118,38], J. Hjorth[144], M. Jauzac[145,80,146,147,99], J. J. E. Kajava[148,149,150], Y. Kang[102], V. Kansal[151,152], D. Karagiannis[111,153], J. Kim[53], C. C. Kirkpatrick[103], A. Kovács[154,155], I. Kovačić[129], K. Koyama[134], S. Kruk[10], M. C. Lam[39], M. Lattanzi[112], L. Legrand[156,9], M. Lembo[141], G. Leroy[145,80], G. F. Lesci[79,2], J. Lesgourgues[157], L. Linke[102], S. J. Liu[50], G. Maggio[14], F. Mannucci[158], F. R. Marleau[102], C. J. A. P. Martins[159,160], M. Miluzio[10,161], G. Morgante[2], S. Nadathur[134], K. Naidoo[134,65], A. Navarro-Alsina[77], A. Nersesian[162,129], S. Nesseris[98], L. Nicastro[2], F. Oppizzi[23,97,96], F. Pace[26,27,28,163], D. Paoletti[2,52], G. Parimbelli[32,16], F. Passalacqua[97], K. Paterson[65], C. Pattison[134], R. Pello[43], A. Pisani[49], D. Potter[164], G. W. Pratt[51], S. Quai[79,2], M. Radovich[19], F. Ricci[165,34], G. Rodighiero[96,19], W. Roster[4], M. Sahlén[166], D. B. Sanders[36], A. Schneider[164], D. Sciotti[34,78], E. Sellentin[167,58], S. Serjeant[168], F. Shankar[169], L. C. Smith[170], S. A. Stanford[171], I. Szapudi[36], M. Talia[79,2], K. Tanidis[172],

C. Tao[49], F. Tarsitano[173,174,3], G. Testera[23], R. Teyssier[175], S. Tosi[22,12,23], A. Troja[14], C. Uhlemann[176,177], C. Valieri[18], A. Venhola[178], D. Vergani[2], P. Vielzeuf[49], S. Vinciguerra[43], M. von Wietersheim-Kramsta[80,145], N. A. Walton[170], L. Wang[179,20], J. R. Weaver[180], and A. H. Wright[7]

[1] CEA Saclay, DFR/IRFU, Service d'Astrophysique, Bat. 709, 91191 Gif-sur-Yvette, France
[2] INAF-Osservatorio di Astrofisica e Scienza dello Spazio di Bologna, Via Piero Gobetti 93/3, 40129 Bologna, Italy
[3] Department of Astronomy, University of Geneva, ch. d'Ecogia 16, 1290 Versoix, Switzerland
[4] Max Planck Institute for Extraterrestrial Physics, Giessenbachstr. 1, 85748 Garching, Germany
[5] Universitäts-Sternwarte München, Fakultät für Physik, Ludwig-Maximilians-Universität München, Scheinerstr. 1, 81679 München, Germany
[6] Department of Physics and Astronomy, University of British Columbia, Vancouver, BC V6T 1Z1, Canada
[7] Ruhr University Bochum, Faculty of Physics and Astronomy, Astronomical Institute (AIRUB), German Centre for Cosmological Lensing (GCCL), 44780 Bochum, Germany
[8] Univ. Lille, CNRS, Centrale Lille, UMR 9189 CRIStAL, 59000 Lille, France
[9] Université Paris-Saclay, CNRS, Institut d'astrophysique spatiale, 91405, Orsay, France
[10] ESAC/ESA, Camino Bajo del Castillo, s/n., Urb. Villafranca del Castillo, 28692 Villanueva de la Cañada, Madrid, Spain
[11] School of Mathematics and Physics, University of Surrey, Guildford, Surrey, GU2 7XH, UK
[12] INAF-Osservatorio Astronomico di Brera, Via Brera 28, 20122 Milano, Italy
[13] IFPU, Institute for Fundamental Physics of the Universe, via Beirut 2, 34151 Trieste, Italy
[14] INAF-Osservatorio Astronomico di Trieste, Via G. B. Tiepolo 11, 34143 Trieste, Italy
[15] INFN, Sezione di Trieste, Via Valerio 2, 34127 Trieste TS, Italy
[16] SISSA, International School for Advanced Studies, Via Bonomea 265, 34136 Trieste TS, Italy
[17] Dipartimento di Fisica e Astronomia, Università di Bologna, Via Gobetti 93/2, 40129 Bologna, Italy
[18] INFN-Sezione di Bologna, Viale Berti Pichat 6/2, 40127 Bologna, Italy
[19] INAF-Osservatorio Astronomico di Padova, Via dell'Osservatorio 5, 35122 Padova, Italy
[20] Kapteyn Astronomical Institute, University of Groningen, PO Box 800, 9700 AV Groningen, The Netherlands
[21] ATG Europe BV, Huygensstraat 34, 2201 DK Noordwijk, The Netherlands
[22] Dipartimento di Fisica, Università di Genova, Via Dodecaneso 33, 16146, Genova, Italy
[23] INFN-Sezione di Genova, Via Dodecaneso 33, 16146, Genova, Italy
[24] Department of Physics "E. Pancini", University Federico II, Via Cinthia 6, 80126, Napoli, Italy
[25] INAF-Osservatorio Astronomico di Capodimonte, Via Moiariello 16, 80131 Napoli, Italy
[26] Dipartimento di Fisica, Università degli Studi di Torino, Via P. Giuria 1, 10125 Torino, Italy
[27] INFN-Sezione di Torino, Via P. Giuria 1, 10125 Torino, Italy
[28] INAF-Osservatorio Astrofisico di Torino, Via Osservatorio 20, 10025 Pino Torinese (TO), Italy
[29] INAF-IASF Milano, Via Alfonso Corti 12, 20133 Milano, Italy
[30] Centro de Investigaciones Energéticas, Medioambientales y Tecnológicas (CIEMAT), Avenida Complutense 40, 28040 Madrid, Spain
[31] Port d'Informació Científica, Campus UAB, C. Albareda s/n, 08193 Bellaterra (Barcelona), Spain
[32] Institute of Space Sciences (ICE, CSIC), Campus UAB, Carrer de Can Magrans, s/n, 08193 Barcelona, Spain
[33] Institut d'Estudis Espacials de Catalunya (IEEC), Edifici RDIT, Campus UPC, 08860 Castelldefels, Barcelona, Spain
[34] INAF-Osservatorio Astronomico di Roma, Via Frascati 33, 00078 Monteporzio Catone, Italy
[35] INFN – Sezione di Napoli, Via Cinthia 6, 80126, Napoli, Italy
[36] Institute for Astronomy, University of Hawaii, 2680 Woodlawn Drive, Honolulu, HI 96822, USA
[37] Dipartimento di Fisica e Astronomia "Augusto Righi" - Alma Mater Studiorum Università di Bologna, Viale Berti Pichat 6/2, 40127 Bologna, Italy
[38] Instituto de Astrofísica de Canarias, E-38205 La Laguna, Tenerife, Spain
[39] Institute for Astronomy, University of Edinburgh, Royal Observatory, Blackford Hill, Edinburgh EH9 3HJ, UK
[40] Jodrell Bank Centre for Astrophysics, Department of Physics and Astronomy, University of Manchester, Oxford Road, Manchester M13 9PL, UK
[41] European Space Agency/ESRIN, Largo Galileo Galilei 1, 00044 Frascati, Roma, Italy
[42] Université Lyon 1, CNRS/IN2P3, IP2I Lyon, Villeurbanne, France
[43] Aix-Marseille Université, CNRS, CNES, LAM, Marseille, France
[44] Institut de Ciències del Cosmos (ICCUB), Universitat de Barcelona (IEEC-UB), Martí i Franquès 1, 08028 Barcelona, Spain
[45] Institució Catalana de Recerca i Estudis Avançats (ICREA), Passeig de Lluís Companys 23, 08010 Barcelona, Spain
[46] Institut de Ciencies de l'Espai (IEEC-CSIC), Campus UAB, Carrer de Can Magrans, s/n Cerdanyola del Vallés, 08193 Barcelona, Spain
[47] Université Lyon 1, CNRS/IN2P3, IUF, IP2I Lyon, Villeurbanne, France
[48] Mullard Space Science Laboratory, University College London, Holmbury St Mary, Dorking, Surrey RH5 6NT, UK
[49] Aix-Marseille Université, CNRS/IN2P3, CPPM, Marseille, France
[50] INAF-Istituto di Astrofisica e Planetologia Spaziali, via del Fosso del Cavaliere, 100, 00100 Roma, Italy
[51] Université Paris-Saclay, Université Paris Cité, CEA, CNRS, AIM, 91191, Gif-sur-Yvette, France
[52] INFN-Bologna, Via Irnerio 46, 40126 Bologna, Italy
[53] Department of Physics, University of Oxford, Keble Road, Oxford OX1 3RH, UK
[54] University Observatory, LMU Faculty of Physics, Scheinerstr. 1, 81679 Munich, Germany
[55] National Research Council, Herzberg Astronomy and Astrophysics Research Centre, 5071 W. Saanich Rd. Victoria, BC, V9E 2E7, Canada
[56] Institute of Theoretical Astrophysics, University of Oslo, P.O. Box 1029 Blindern, 0315 Oslo, Norway
[57] Caltech/IPAC, 1200 E. California Blvd., Pasadena, CA 91125, USA
[58] Leiden Observatory, Leiden University, Einsteinweg 55, 2333 CC Leiden, The Netherlands
[59] Jet Propulsion Laboratory, California Institute of Technology, 4800 Oak Grove Drive, Pasadena, CA, 91109, USA
[60] Felix Hormuth Engineering, Goethestr. 17, 69181 Leimen, Germany
[61] Technical University of Denmark, Elektrovej 327, 2800 Kgs. Lyngby, Denmark
[62] Cosmic Dawn Center (DAWN), Denmark

[63] Université PSL, Observatoire de Paris, Sorbonne Université, CNRS, LERMA, 75014, Paris, France
[64] Université Paris-Cité, 5 Rue Thomas Mann, 75013, Paris, France
[65] Max-Planck-Institut für Astronomie, Königstuhl 17, 69117 Heidelberg, Germany
[66] NASA Goddard Space Flight Center, Greenbelt, MD 20771, USA
[67] Department of Physics and Astronomy, University College London, Gower Street, London WC1E 6BT, UK
[68] Université de Genève, Département de Physique Théorique and Centre for Astroparticle Physics, 24 quai Ernest-Ansermet, CH-1211 Genève 4, Switzerland
[69] Department of Physics, P.O. Box 64, University of Helsinki, 00014 Helsinki, Finland
[70] Helsinki Institute of Physics, Gustaf Hällströmin katu 2, University of Helsinki, 00014 Helsinki, Finland
[71] Laboratoire d'etude de l'Univers et des phenomenes eXtremes, Observatoire de Paris, Université PSL, Sorbonne Université, CNRS, 92190 Meudon, France
[72] SKAO, Jodrell Bank, Lower Withington, Macclesfield SK11 9FT, UK
[73] Centre de Calcul de l'IN2P3/CNRS, 21 avenue Pierre de Coubertin 69627 Villeurbanne Cedex, France
[74] Dipartimento di Fisica "Aldo Pontremoli", Università degli Studi di Milano, Via Celoria 16, 20133 Milano, Italy
[75] INFN-Sezione di Milano, Via Celoria 16, 20133 Milano, Italy
[76] University of Applied Sciences and Arts of Northwestern Switzerland, School of Computer Science, 5210 Windisch, Switzerland
[77] Universität Bonn, Argelander-Institut für Astronomie, Auf dem Hügel 71, 53121 Bonn, Germany
[78] INFN-Sezione di Roma, Piazzale Aldo Moro, 2 - c/o Dipartimento di Fisica, Edificio G. Marconi, 00185 Roma, Italy
[79] Dipartimento di Fisica e Astronomia "Augusto Righi" - Alma Mater Studiorum Università di Bologna, via Piero Gobetti 93/2, 40129 Bologna, Italy
[80] Department of Physics, Institute for Computational Cosmology, Durham University, South Road, Durham, DH1 3LE, UK
[81] Infrared Processing and Analysis Center, California Institute of Technology, Pasadena, CA 91125, USA
[82] Université Paris Cité, CNRS, Astroparticule et Cosmologie, 75013 Paris, France
[83] CNRS-UCB International Research Laboratory, Centre Pierre Binétruy, IRL2007, CPB-IN2P3, Berkeley, USA
[84] University of Applied Sciences and Arts of Northwestern Switzerland, School of Engineering, 5210 Windisch, Switzerland
[85] Institute of Physics, Laboratory of Astrophysics, Ecole Polytechnique Fédérale de Lausanne (EPFL), Observatoire de Sauverny, 1290 Versoix, Switzerland
[86] Dipartimento di Fisica - Sezione di Astronomia, Università di Trieste, Via Tiepolo 11, 34131 Trieste, Italy
[87] Telespazio UK S.L. for European Space Agency (ESA), Camino bajo del Castillo, s/n, Urbanizacion Villafranca del Castillo, Villanueva de la Cañada, 28692 Madrid, Spain
[88] Institut de Física d'Altes Energies (IFAE), The Barcelona Institute of Science and Technology, Campus UAB, 08193 Bellaterra (Barcelona), Spain
[89] European Space Agency/ESTEC, Keplerlaan 1, 2201 AZ Noordwijk, The Netherlands
[90] Waterloo Centre for Astrophysics, University of Waterloo, Waterloo, Ontario N2L 3G1, Canada
[91] Department of Physics and Astronomy, University of Waterloo, Waterloo, Ontario N2L 3G1, Canada
[92] Perimeter Institute for Theoretical Physics, Waterloo, Ontario N2L 2Y5, Canada
[93] Space Science Data Center, Italian Space Agency, via del Politecnico snc, 00133 Roma, Italy
[94] Centre National d'Etudes Spatiales – Centre spatial de Toulouse, 18 avenue Edouard Belin, 31401 Toulouse Cedex 9, France
[95] Institute of Space Science, Str. Atomistilor, nr. 409 Măgurele, Ilfov, 077125, Romania
[96] Dipartimento di Fisica e Astronomia "G. Galilei", Università di Padova, Via Marzolo 8, 35131 Padova, Italy
[97] INFN-Padova, Via Marzolo 8, 35131 Padova, Italy
[98] Instituto de Física Teórica UAM-CSIC, Campus de Cantoblanco, 28049 Madrid, Spain
[99] Institut de Recherche en Astrophysique et Planétologie (IRAP), Université de Toulouse, CNRS, UPS, CNES, 14 Av. Edouard Belin, 31400 Toulouse, France
[100] Université St Joseph; Faculty of Sciences, Beirut, Lebanon
[101] Departamento de Física, FCFM, Universidad de Chile, Blanco Encalada 2008, Santiago, Chile
[102] Universität Innsbruck, Institut für Astro- und Teilchenphysik, Technikerstr. 25/8, 6020 Innsbruck, Austria
[103] Department of Physics and Helsinki Institute of Physics, Gustaf Hällströmin katu 2, University of Helsinki, 00014 Helsinki, Finland
[104] Departamento de Física, Faculdade de Ciências, Universidade de Lisboa, Edifício C8, Campo Grande, PT1749-016 Lisboa, Portugal
[105] Instituto de Astrofísica e Ciências do Espaço, Faculdade de Ciências, Universidade de Lisboa, Tapada da Ajuda, 1349-018 Lisboa, Portugal
[106] Cosmic Dawn Center (DAWN)
[107] Niels Bohr Institute, University of Copenhagen, Jagtvej 128, 2200 Copenhagen, Denmark
[108] Universidad Politécnica de Cartagena, Departamento de Electrónica y Tecnología de Computadoras, Plaza del Hospital 1, 30202 Cartagena, Spain
[109] European University of Technology EUt+, European Union
[110] Astronomisches Rechen-Institut, Zentrum für Astronomie der Universität Heidelberg, Mönchhofstr. 12-14, 69120 Heidelberg, Germany
[111] Dipartimento di Fisica e Scienze della Terra, Università degli Studi di Ferrara, Via Giuseppe Saragat 1, 44122 Ferrara, Italy
[112] Istituto Nazionale di Fisica Nucleare, Sezione di Ferrara, Via Giuseppe Saragat 1, 44122 Ferrara, Italy
[113] ICSC - Centro Nazionale di Ricerca in High Performance Computing, Big Data e Quantum Computing, Via Magnanelli 2, Bologna, Italy
[114] INAF, Istituto di Radioastronomia, Via Piero Gobetti 101, 40129 Bologna, Italy
[115] Astronomical Observatory of the Autonomous Region of the Aosta Valley (OAVdA), Loc. Lignan 39, I-11020, Nus (Aosta Valley), Italy
[116] Université Côte d'Azur, Observatoire de la Côte d'Azur, CNRS, Laboratoire Lagrange, Bd de l'Observatoire, CS 34229, 06304 Nice cedex 4, France
[117] Department of Mathematical Physics, Institute of Physics, University of São Paulo, R. do Matão 1371, 05508-090, São Paulo, SP, Brazil
[118] Universidad de La Laguna, Dpto. Astrofísica, E-38206 La Laguna, Tenerife, Spain
[119] Oskar Klein Centre for Cosmoparticle Physics, Department of Physics, Stockholm University, Stockholm, SE-106 91, Sweden
[120] Astrophysics Group, Blackett Laboratory, Imperial College London, London SW7 2AZ, UK
[121] Univ. Grenoble Alpes, CNRS, Grenoble INP, LPSC-IN2P3, 53, Avenue des Martyrs, 38000 Grenoble, France
[122] Dipartimento di Fisica, Sapienza Università di Roma, Piazzale Aldo Moro 2, 00185 Roma, Italy
[123] Institut d'Astrophysique de Paris, 98bis Boulevard Arago, 75014, Paris, France

[124] ICL, Junia, Université Catholique de Lille, LITL, 59000 Lille, France
[125] CERCA/ISO, Department of Physics, Case Western Reserve University, 10900 Euclid Avenue, Cleveland, OH 44106, USA
[126] Laboratoire Univers et Théorie, Observatoire de Paris, Université PSL, Université Paris Cité, CNRS, 92190 Meudon, France
[127] Departamento de Física Fundamental. Universidad de Salamanca. Plaza de la Merced s/n. 37008 Salamanca, Spain
[128] IRFU, CEA, Université Paris-Saclay 91191 Gif-sur-Yvette Cedex, France
[129] Universiteit Gent, Department of Physics and Astronomy, Proeftuinstraat 86 N3, 9000 Ghent, Belgium
[130] Université de Strasbourg, CNRS, Observatoire astronomique de Strasbourg, UMR 7550, 67000 Strasbourg, France
[131] Center for Data-Driven Discovery, Kavli IPMU (WPI), UTIAS, The University of Tokyo, Kashiwa, Chiba 277-8583, Japan
[132] Max-Planck-Institut für Physik, Boltzmannstr. 8, 85748 Garching, Germany
[133] California Institute of Technology, 1200 E California Blvd, Pasadena, CA 91125, USA
[134] Institute of Cosmology and Gravitation, University of Portsmouth, Portsmouth PO1 3FX, UK
[135] Department of Physics & Astronomy, University of California Irvine, Irvine CA 92697, USA
[136] Departamento Física Aplicada, Universidad Politécnica de Cartagena, Campus Muralla del Mar, 30202 Cartagena, Murcia, Spain
[137] Instituto de Física de Cantabria, Edificio Juan Jordá, Avenida de los Castros, 39005 Santander, Spain
[138] Department of Mathematics and Physics E. De Giorgi, University of Salento, Via per Arnesano, CP-I93, 73100, Lecce, Italy
[139] INFN, Sezione di Lecce, Via per Arnesano, CP-193, 73100, Lecce, Italy
[140] INAF-Sezione di Lecce, c/o Dipartimento Matematica e Fisica, Via per Arnesano, 73100, Lecce, Italy
[141] Institut d'Astrophysique de Paris, UMR 7095, CNRS, and Sorbonne Université, 98 bis boulevard Arago, 75014 Paris, France
[142] Department of Computer Science, Aalto University, PO Box 15400, Espoo, FI-00 076, Finland
[143] School of Physics and Astronomy, University of Nottingham, University Park, Nottingham NG7 2RD, UK
[144] DARK, Niels Bohr Institute, University of Copenhagen, Jagtvej 155, 2200 Copenhagen, Denmark
[145] Department of Physics, Centre for Extragalactic Astronomy, Durham University, South Road, Durham, DH1 3LE, UK
[146] Astrophysics Research Centre, University of KwaZulu-Natal, Westville Campus, Durban 4041, South Africa
[147] School of Mathematics, Statistics & Computer Science, University of KwaZulu-Natal, Westville Campus, Durban 4041, South Africa
[148] Department of Physics and Astronomy, Vesilinnantie 5, University of Turku, 20014 Turku, Finland
[149] Finnish Centre for Astronomy with ESO (FINCA), Quantum, Vesilinnantie 5, University of Turku, 20014 Turku, Finland
[150] Serco for European Space Agency (ESA), Camino bajo del Castillo, s/n, Urbanizacion Villafranca del Castillo, Villanueva de la Cañada, 28692 Madrid, Spain
[151] ARC Centre of Excellence for Dark Matter Particle Physics, Melbourne, Australia
[152] Centre for Astrophysics & Supercomputing, Swinburne University of Technology, Hawthorn, Victoria 3122, Australia
[153] Department of Physics and Astronomy, University of the Western Cape, Bellville, Cape Town, 7535, South Africa
[154] MTA-CSFK Lendület Large-Scale Structure Research Group, Konkoly-Thege Miklós út 15-17, H-1121 Budapest, Hungary
[155] Konkoly Observatory, HUN-REN CSFK, MTA Centre of Excellence, Budapest, Konkoly Thege Miklós út 15-17. H-1121, Hungary
[156] Brazilian Center for Research in Physics (CBPF), Dr. Xavier Sigaud st. 150, zip 22290-180, Rio de Janeiro, RJ, Brazil
[157] Institute for Theoretical Particle Physics and Cosmology (TTK), RWTH Aachen University, 52056 Aachen, Germany
[158] INAF-Osservatorio Astrofisico di Arcetri, Largo E. Fermi 5, 50125, Firenze, Italy
[159] Centro de Astrofísica da Universidade do Porto, Rua das Estrelas, 4150-762 Porto, Portugal
[160] Instituto de Astrofísica e Ciências do Espaço, Universidade do Porto, CAUP, Rua das Estrelas, PT4150-762 Porto, Portugal
[161] HE Space for European Space Agency (ESA), Camino bajo del Castillo, s/n, Urbanizacion Villafranca del Castillo, Villanueva de la Cañada, 28692 Madrid, Spain
[162] STAR Institute, University of Liège, Quartier Agora, Allée du six Août 19c, 4000 Liège, Belgium
[163] Instituto de Astrofísica e Ciências do Espaço, Faculdade de Ciências, Universidade de Lisboa, Campo Grande, 1749-016 Lisboa, Portugal
[164] Department of Astrophysics, University of Zurich, Winterthurerstrasse 190, 8057 Zurich, Switzerland
[165] Department of Mathematics and Physics, Roma Tre University, Via della Vasca Navale 84, 00146 Rome, Italy
[166] Theoretical astrophysics, Department of Physics and Astronomy, Uppsala University, Box 524, 751 20 Uppsala, Sweden
[167] Mathematical Institute, University of Leiden, Einsteinweg 55, 2333 CA Leiden, The Netherlands
[168] School of Physical Sciences, The Open University, Milton Keynes, MK7 6AA, UK
[169] School of Physics & Astronomy, University of Southampton, Highfield Campus, Southampton SO17 1BJ, UK
[170] Institute of Astronomy, University of Cambridge, Madingley Road, Cambridge CB3 0HA, UK
[171] Department of Physics and Astronomy, University of California, Davis, CA 95616, USA
[172] Center for Astrophysics and Cosmology, University of Nova Gorica, Nova Gorica, Slovenia
[173] Kobayashi-Maskawa Institute for the Origin of Particles and the Universe, Nagoya University, Chikusa-ku, Nagoya, 464-8602, Japan
[174] Institute for Particle Physics and Astrophysics, Dept. of Physics, ETH Zurich, Wolfgang-Pauli-Strasse 27, 8093 Zurich, Switzerland
[175] Department of Astrophysical Sciences, Peyton Hall, Princeton University, Princeton, NJ 08544, USA
[176] Fakultät für Physik, Universität Bielefeld, Postfach 100131, 33501 Bielefeld, Germany
[177] School of Mathematics, Statistics and Physics, Newcastle University, Herschel Building, Newcastle-upon-Tyne, NE1 7RU, UK
[178] Space physics and astronomy research unit, University of Oulu, Pentti Kaiteran katu 1, FI-90014 Oulu, Finland
[179] SRON Netherlands Institute for Space Research, Landleven 12, 9747 AD, Groningen, The Netherlands
[180] MIT Kavli Institute for Astrophysics and Space Research, Massachusetts Institute of Technology, Cambridge, MA 02139, USA

⋆ e-mail: andrea.enia@cea.fr